RUPRECHT-KARLS-UNIVERSITÄT HEIDELBERG

Jan-Patrick Porst

Towards MARE: Development of a Metallic Magnetic Calorimeter with Superconducting Rhenium Absorber

Diploma Thesis

HD-KIP 07-11

KIRCHHOFF-INSTITUT FÜR PHYSIK

Faculty of Physics and Astronomy
University of Heidelberg

Diploma Thesis
in Physics

submitted by
Jan-Patrick Porst
born in Pretoria

2007

Towards MARE:
Development of a Metallic Magnetic Calorimeter with Superconducting Rhenium Absorber

This diploma thesis has been carried out by Jan-Patrick Porst
at the Kirchhoff Institute for Physics
under the supervision of
Professor Christian Enss

This thesis describes the development of a metallic magnetic calorimeter (MMC) with a superconducting rhenium absorber. A magnetic calorimeter is an energy dispersive particle detector, which is operated at temperatures below 100 mK and makes use of a paramagnetic temperature sensor positioned in a weak magnetic field. A temperature change upon the deposition of energy causes a change in the magnetization of the sensor. Monitoring this change using a low-noise SQUID magnetometer one obtains an accurate measure of the deposited energy. The work is carried out within the context of MARE (**M**ircocalorimeter **A**rrays for a **R**henium **E**xperiment), an experiment for measuring the β-decay of ^{187}Re with the objective to determine the neutrino mass with a sensitivity better than $0.2\,\mathrm{eV/c^2}$.
The detector developed in this work is studied with particular emphasis on the properties of rhenium as a superconductor and the thermalization behavior within this absorber. It is demonstrated that the transition temperature of the superconducting rhenium as well as its resistivity in the normal conducting state can be measured in situ. The detector response has been characterized at a number of operating temperatures and magnetic fields by using 5.9 keV photons. The signal shapes are discussed on the basis of a thermodynamic model that comprises thermal as well as athermal processes within the superconducting absorber.

Entwicklung eines magnetischen Kalorimeters mit supraleitendem Rhenium Absorber für MARE

In der vorliegenden Diplomarbeit wurde ein metallisches magnetisches Kalorimeter mit supraleitdendem Rhenium Absorber entwickelt. Ein magnetisches Kalorimeter ist ein energiedispersiver Teilchendetektor, der bei Temperaturen unter 100 mK betrieben wird und als Temperatursensor eine paramagnetische Legierung in einem schwachen Magnetfeld verwendet. Eine auf einen Energieeintrag folgende Temperaturerhöhung des Sensors führt zu einer Änderung dessen Magnetisierung. Diese kann mit Hilfe eines rauscharmen SQUID-Magnetometers nachgewiesen werden und gibt ein präzises Maß für die in den Detektor eingetragene Energie. Die Arbeit steht im Rahmen von MARE (**M**ircocalorimeter **A**rrays for a **R**henium **E**xperiment), ein Experiment zur Messung des β-Zerfalls von ^{187}Re, mit dem Ziel eine Nachweisgrenze der Neutrinomasse von unter $0,2\,\mathrm{eV/c^2}$ zu erreichen.
Bei der Untersuchung des in dieser Arbeit entwickelten Detektors wird besonderes Augenmerk auf die Eigenschaften des supraleitenden Rhenium Absorbers gelegt. Es wird gezeigt, dass sowohl die Sprungtemperatur zur Supraleitung, als auch der spezifische Widerstand des Rhenium Absorbers im normalleitenden Zustand in situ ermittelt werden kann. Der zeitliche Verlauf des Detektorsignals nach der Absorption von einzelnen Röntgenquanten der Energie $5,9\,\mathrm{keV}$ wurde für verschiedene Betriebstemperaturen und Magnetfelder gemessen. Die Signalformen werden anhand eines thermodynamischen Models, das sowohl thermische als auch athermische Prozesse innerhalb des supraleitenden Absorbers beinhaltet, diskutiert.

Contents

1. Introduction

The neutrino is one of the fundamental particles which make up the universe. Among the elementary particles it is one of the least understood. In 1930 W. Pauli first theoretically introduced the neutrino as a desperate remedy for an otherwise not fulfilled energy conservation. The theoretical particle he described had properties that made it so elusive that even Pauli wondered whether anyone would ever observe it. So he himself commented on this as "I have done something very bad today in proposing a particle that cannot be detected".

First experimental proof of the existence of neutrinos was given by F. Reines and C. Cowan in 1953. Somewhat later, in experiments detecting solar and atmospheric neutrinos evidence for neutrino flavor oscillations were found. In this framework the neutrino nowadays is widely accepted to carry nonzero mass. Yet, the absolute mass of the neutrino is unknown so far. Different physical approaches address this topic ranging from cosmological investigations to the cradle of the neutrino – the β-decay and its kinematics. Determining the rest mass of the neutrino currently is one of the most desired quests of neutrino physics as it not only tells us more about the nature of the neutrino itself, but also illuminates the path towards new physics beyond the Standard Model.

Since the Seventies of the last century measurement of the spectrum of the tritium β-decay were undertaken by means of magnetic spectrometers. With these measurements the upper limit of the neutrino mass was soon pushed to limits where the requirements for the energetically resolved detection of emitted electrons becomes very demanding.

As a complementary experimental approach the investigation of the β-decay of ^{187}Re with low temperature microcalorimeters was proposed by D. McCammon [McC85] and S. Vitale [Vit84] in 1985. Already in the Nineties first promising results where achieved with semiconducting thermistors [San06]. The calorimetric approach and questions to solid states physics raised by the development of faster detectors with an higher energy resolution are currently under investigation.

This work is located within this framework; a metallic magnetic calorimeter (MMC) with a superconducting rhenium absorber was studied. In this detection scheme a paramagnetic temperature sensor is placed in a weak magnetic field. The sensor material used is a dilute alloy of erbium in gold. Any energy input leads to a change in magnetization in the sensor material which is read out with a dc-SQUID. The developed detector is studied with particular emphasis on the properties of rhenium as a superconductor and the thermalization behavior within the superconducting absorber.

Chapter 2 addresses some major points of neutrino physics important for the direct determination of the neutrino mass. Two presently active experiments examining the spectrum of a single β-decay are described; KATRIN and MARE, investigating the β-decay spectrum of tritium and ^{187}Re, respectively. Requirements for

the MARE experiment to achieve a detection limit for the neutrino mass competitive to those of the KATRIN experiment are presented.

Chapter 3 discusses the detection principle of magnetic calorimeters and the fundamental limitation on the energy resolution. The thermodynamic properties of the paramagnetic sensor material are presented. Furthermore some thermodynamic properties of the absorber material rhenium are summarized. The consequences of rhenium being superconducting at typical working temperatures of the calorimeter are discussed, including a review of the possible thermalization mechanisms in a superconductor. Additionally the detector geometry with a meander shaped pickup coil used in our experiment is introduced. It is shown how to calculate the expected signalsize for this detector geometry as a function of operational parameters. In addition the different contributions to the detector signal noise are discussed, especially emphasizing on finite elements calculations to estimate the spectral shape of magnetic Johnson noise in the SQUID that is generated by thermal currents in normal conducting parts of the detector.

Chapter 4 describes the experimental methods. The cryogenics which were used to achieve the required operation temperature of the detector are introduced. The working principle of dc-SQUID magnetometers is described in general and illustrated with measurements of the SQUIDs, used in our experiments. Furthermore, the design of the detector is reported in detail. It comprises of a microfabricated meander shaped coil generating the magnetic field for the paramagnetic sensor. The sensor it glued on this SQUID chip. Finally the rhenium absorber is glued on the sensor only separated by a spacer layer made of gold.

Chapter 5 contains the experimental results. It is demonstrated that the transition temperature of rhenium can be measured with two in situ methods, one based on the measurement of noise and another one based on measuring mutual inductances. This is indeed an important feature of this kind of setup, because the superconducting properties of single crystal rhenium depend strongly on mechanical stress. Deformations of the crystals due to this can be cured by heat treatment. One of the developed detectors is characterized by means of magnetization measurements of as a function of temperature for different magnetic fields. The signal shape recorded upon the deposition of single X-rays are analyzed for different magnetic fields at varying temperature of the detector. A thermodynamic model for the thermalization in the superconducting rhenium absorber is proposed and the data are analyzed accordingly. From this, parameters like thermal conductances, heat capacities and branching ratios of the energy in a thermal system, quasiparticles and athermal ballistic phonons are derived. The results obtained by the analyses are summarized and an outlook is given, including some specific suggestions for future experiments.

2. Searching the Neutrino Mass

2.1 The Nature of the Neutrino

In a β-decay the weak interaction converts a neutron into a proton. Experiments performed by L. Meitner and O. Hahn in 1911 showed that the electron emitted in a β-decay has a continuous rather than a discrete energy spectrum, as it would be expected for the transformation of one element X into another one X$'$ with just the emission of an electron. This was the first evidence for this decay to have three products. In his famous letter (1930 [Pau30]) to the "Dear Radioactive Ladies and Gentlemen" W. Pauli postulated the existence of a particle with zero electric charge, spin 1/2 and at least being lighter than an electron – the neutrino.

$$ {}^{A}_{Z}X \longrightarrow {}^{A}_{Z+1}X' + e^- + \overline{\nu}_{\mathrm{e}}. \tag{2.1} $$

Here A denotes the nucleon number and Z stands for the number of protons in the nucleus. This suggested particle was to cure the conservation of energy and angular momentum in the beta decay. In retrospect the neutrino was also required to fulfill the conservation of lepton number in the β-decay. E. Fermi developed the first theory including the neutrino in a β-decay in 1934. Because this postulated fermion only interacts weakly and via gravity, it took another 22 years until the first experimental proof of the neutrino's existence was given by C.L. Reines and F. Cowan (1956) in a reverse β-decay experiment [Cow56]. Later the neutrino was included sixfold (there being three neutrino generations and their antiparticle counterparts, the antineutrinos) as a massless particle in the Standard Model.

The so called solar neutrino problem then was the next milestone in the history of the neutrino. It is the discrepancy between the number of electron neutrinos measured to travel to the earth and this number calculated from theoretical solar models. Nowadays this discrepancy is explained with neutrino oscillations first proposed by Maki *et al.*[Mak62]. Neutrino oscillations imply that a neutrino created with a specific weak interaction flavor, e.g. electron-, muon- or tau-neutrino can later be measured to be in another weak interaction flavor eigenstate. The existence of neutrino oscillations requires a non trivial mixing between the weak interaction states (ν_e, ν_μ, ν_τ) and the corresponding neutrino mass eigenstates (ν_1, ν_2, ν_3) and moreover that the masses differ from each other. The probability at time t that a neutrino with initial flavor ν_α is observed as a neutrino of flavor ν_β is [Rou04]

$$ P_{\nu_\alpha \to \nu_\beta}(t) = |\langle \nu_\beta | \nu(t) \rangle|^2 = \left| \sum_k V^*_{\alpha k} e^{-i \frac{m_k^2}{2E} t} V_{\beta k} \right|^2 , \tag{2.2} $$

where V is the neutrino mixing matrix, E is the energy of neutrinos and m_k is the mass. Considering only two flavors the mixing matrix can be expressed as a rotation

with a mixing angle θ and equation (2.2) simplifies to

$$P_{\nu_\alpha \to \nu_\beta} = \sin^2 2\theta \sin^2 \left(\frac{\Delta m^2 L}{4E} \right) \tag{2.3}$$

which depends on the difference of the squared masses $\Delta m^2 = m_2^2 - m_1^2$, the mixing angle θ, the energy of the neutrino and the distance L travelled. Experiments at the Sudbury Neutrino Observatory (SNO) could distinguish between events induced by the different neutrino flavors *and* count the neutrino flux coming from the sun. The results for the total number of neutrinos agreed quite well with the prognosis but only 35% of all neutrinos appeared to be electron neutrinos thus giving strong evidence for neutrino oscillations and herewith the existence of a nonzero neutrino mass.

At present the finite mass of the neutrino is accepted as being the first serious shortcoming in the Standard Model. From oscillation experiments the difference of the squared masses Δm_{ij}^2 can be estimated. Still this does not provide information about the hierarchy of the neutrino masses and the absolute scale of those. To get an estimate on the absolute neutrino masses direct measurements are needed.

2.2 Direct Investigation of the Neutrino Mass

Now knowing that the beta decay is a three body decay a continuous energy spectrum is expected for the electron as well as for the neutrino. The larger the mass of the neutrino will be, the less kinetic energy will be available for the escaping electron and herewith the spectrum will be altered.

Following Fermi's golden rule the spectrum of such a decay can be determined to be of the form

$$N(E_\mathrm{e})\mathrm{d}E_\mathrm{e} = S(E_\mathrm{e})F(Z', E_\mathrm{e})E_\mathrm{e}p_\mathrm{e}(E_0 - E_\mathrm{e})^2\mathrm{d}E_\mathrm{e}, \tag{2.4}$$

here E_0 is the total energy available in the decay, it is given by the mass difference of the nuclei X and X'. E_e and p_e represent the total energy and momentum carried by the emitted electron. $S(E_\mathrm{e})$ is the form factor and $F(Z', E_\mathrm{e})$ is the Fermi function also considering the Coulomb interaction of the emitted electron with the remaining charge $Z'e$. The overall shape is determined by the phase space factor $E_\mathrm{e}p_\mathrm{e}(E_0 - E_\mathrm{e})^2$. If a finite neutrino mass is taken into account the phase space factor needs to be corrected to the reduced endpoint energy, the correction needed is determined by the rest mass of the neutrino $E_\nu^\mathrm{r} = m_\nu c^2$.

Including this, the influence of a finite neutrino mass is better pictured in the so called Kurie plot in which the square root of the number of β-particles whose energies lie within a certain narrow range, divided by the Fermi function, is plotted against β-particle energy

$$K(E_\mathrm{e}) = \sqrt{\frac{N(E_\mathrm{e})}{S(E_\mathrm{e})F(Z', E_\mathrm{e})E_\mathrm{e}p_\mathrm{e}}} \propto \sqrt{(E_0 - E_\mathrm{e})\sqrt{(E_0 - E_\mathrm{e})^2 - m_{\nu_\mathrm{e}}^2 c^4}}. \tag{2.5}$$

For a neutrino with zero mass this is a straight line intersecting the energy axis at E_0. A finite neutrino mass leads to a deviation from this linearity and the endpoint lies at $E = E_0 - m_{\nu_e}c^2$ as illustrated in Figure 2.1. Most of the information on the neutrino mass is therefore contained in the high energy part of the Kurie plot where the count rate unfortunately is low, the fraction of events in the relevant energy regime close to the endpoint of the spectrum is

$$F(\delta E) = \frac{1}{N} \int_{E_0-\delta E}^{E_0} N(E_e, m_{\nu_e} = 0)\mathrm{d}E \approx 2\left(\frac{\delta E}{E_0}\right)^3. \tag{2.6}$$

The number of counts most revealing for the neutrino mass decreases with the third power of the end-point energy. Thus it will be of advantage to analyze beta decays with lowest possible end-point energies. Two isotopes that meet this requirement are under current investigation: the radioactive hydrogen isotope tritium (^{3}H) with E_0 of 18.6 keV and rhenium (^{187}Re) having the lowest known end-point energy at 2.47 keV.

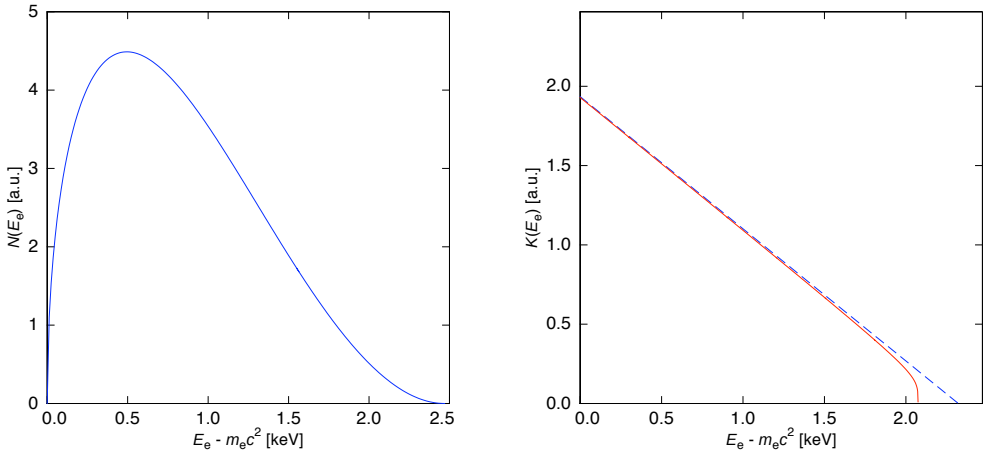

Figure 2.1 Left: spectral shape of ^{187}Re β-decay. Right: Kurie plot of ^{187}Re spectrum with massless neutrino (dashed line) and an assumed neutrino mass $m_\nu = 50$ eV

For investigations of a neutrino mass in the eV range, only events within the last few eV of the spectrum contain the necessary information. Applying (2.6) to tritium ($E_0 = 18.6$ keV) the resulting useful fraction of events within the last 10 eV of the spectrum is only $3 \cdot 10^{-10}$ and gives a first impression on how delicate direct neutrino mass measurements are.

2.2.1 The KATRIN Experiment

Already in the Sixties of the last century experiments on the determination of the neutrino mass in the tritium beta decay were carried out employing magnetic or electrostatic spectrometers. The high energy resolution of the Mainz and Troitsk experiments, reaching upper limits of $m_\nu \leq 2.2\,\mathrm{eV/c^2}$ [Bon02] and $m_\nu \leq 2.05\,\mathrm{eV/c^2}$

[Lob03] respectively (with a 95% confidence level) were due to the development of a new type of spectrometers – the MAC-E filter[1][Lob85].

In this kind of spectrometer, the electrons isotropically emitted in a beta decay are transformed into a broad beam flying almost parallel to the magnetic field lines, as shown in Figure 2.2. This beam of electrons runs against an electrostatic potential. Just those electrons overcoming this threshold will be reaccelerated and collimated onto the detector. Therefore the MAC-E filter acts as an integrating high-energy pass filter.

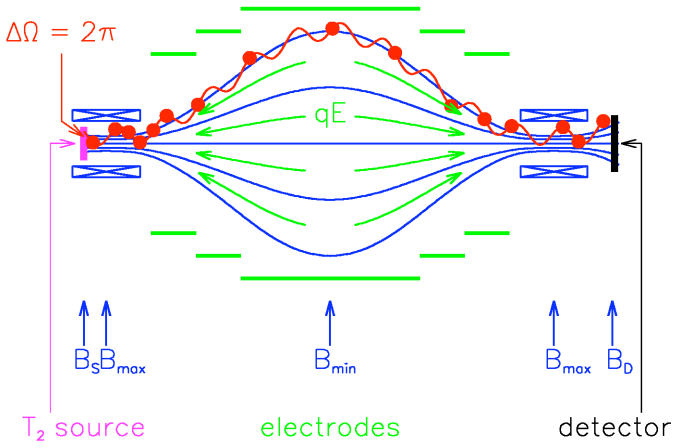

Figure 2.2 Scheme of a MAC-E filter

This technique will be employed again in the upcoming large **Ka**rlsruhe **Tri**tium **n**eutrino (KATRIN) experiment. The successor of the Mainz and Troitsk experiments will benefit from the better understanding of systematical uncertainties. It also features a larger and improved spectrometer leading to a higher energy resolution. Also a higher statistics will be achieved by a tenfold measuring period and a stronger tritium source. The KATRIN experiment aims at lowering the upper limit of the neutrino mass by one order of magnitude (2 eV → 0.2 eV).

There are some evident downsides for a setup of that kind. For example the source will always be external, which as a consequence allows a transition to an excited state of the produced helium nucleus. In the detector this decay will not be distinguishable from a decay to the ground state and thus gives rise to a potential loss in detected energy. The undeniable advantages of KATRIN to the methods introduced in the following which should be kept in mind. For the KATRIN experiment a high energy resolution of the order of 1 eV can be achieved. It is possible to select only those electrons close enough to the transition energy allowing a high activity source. With this it is possible to concentrate on the most relevant part of the Kurie plot and high statistics can be achieved.

[1] Magnetic Adiabatic Collimation with an Electrostatic filter

2.2.2 The MARE[2] Project

Now an alternative laboratory experiment for a direct neutrino mass measurement will be presented, which is under development to achieve complementary results to those of the KATRIN experiment. This approach is to embed the source into the detector and to carry out a calorimetric measurement of the decay energy. Only the neutrino will be able to escape from the detector so this leads to a direct measurement of the desired quantity namely the total decay energy minus the energy carried away by the neutrino. For an experiment of this kind the isotope ^{187}Re with the lowest known Q value and a long half life is advantageous. Low temperature microcalorimeters operated at temperatures below $T = 100\,\mathrm{mK}$ are proposed as detectors.

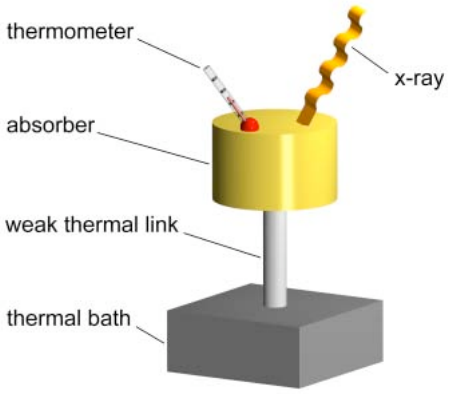

Figure 2.3 Basic principle of a calorimeter

The underlying general principle of a calorimeter is pictured in Figure 2.3. The detector consists of an absorber suited for the particles to be detected which is strongly coupled to a thermometer which precisely monitors the absorber's temperature. Both together form the calorimeter which is weakly coupled to a thermal bath. The energy E deposited in an absorber is determined via the temperature rise of the detector of given heat capacity C_{tot}

$$\delta T = \frac{E}{C_{\mathrm{tot}}}. \tag{2.7}$$

The signature of such an event usually is the fast temperature rise followed by a decay. The decay time is determined by the heat capacities and the thermal conductances G involved:

$$\Delta T(t) \propto E/C \exp(-t/\tau) \quad \text{with} \quad \tau = C_{\mathrm{tot}}/G. \tag{2.8}$$

Currently there are three methods for a precise temperature read out under investigation in order to read out the temperature rise of a microcalorimeter with an absorber containing ^{187}Re

[2]Microcalorimeter Arrays for a Rhenium Experiment

- Semiconductor Thermistors [McC05],
- Superconducting Transition Edge Sensors (TES) [Irw05],
- Metallic Magnetic Calorimeters (MMC) [Fle05]

the latter of those was utilized in the work for this thesis.

A calorimetric detector certainly benefits from the total absorption design, by this energy losses in the source and systematic uncertainties due to decays to excited final states are avoided. Still one should already at this level be aware of some difficulties involved in calorimetric detectors. For this kind of experiment the challenges due to pile-up events and Beta Environmental Fine Structure (BEFS), a known solid state effect, will be discussed to give some idea of the problems involved.

Maybe the most challenging task for calorimeters is to cope with the so called pile-up rate. Depending on the detector there will be a limited resolving time τ_R of pulse pairs, which will be on the order of the detector's rise time. If now the separation of two pulses in time is greater than this a pile-up will always be recognized. In case it is smaller the incoming pulse will not be interpreted correctly. The fraction of unresolved pile-up events will be approximately the product of the total activity A of the source and the pulse pair resolving time τ_R

$$f_{pu} \approx A\tau_R \tag{2.9}$$

and hence the coincidence rate will be approximately $A^2\tau_R$.

The approach using a solid rhenium absorber also brings some challenges. It is needless to say that the physics involved on the microscopic scale in the absorption of a β-particle in the rhenium will be hard to understand since we deal with all degrees of freedom involved in a solid state. The potential use of pure rhenium absorbers additionally introduces superconducting properties to be investigated.

For a neutrino mass experiment the β-decay of the studied source needs to be well understood. 1991 Koonin [Koo91] found there should be structure in the β-spectrum depending on the atomic surrounding of the decaying nucleus. He called this Beta Environmental Fine Structure (BEFS). This effect of the crystalline environment on the energy spectrum for the β-decay of nuclei in a crystal has been observed by Gatti [Gat99] in metallic rhenium. It will need further study to understand the systematic influence of BEFS on the spectrum of ^{187}Re. At present the effect is known to be detectable at low energies while the effect near the end-point is likely to be negligible.

In the search for a finite neutrino mass the principle of low temperature calorimeters is followed since the early Nineties of last century in the investigation of the β-decay of ^{187}Re. The best published calorimetric limit was measured with silicon implanted thermistors and came out to be $m_\nu \leq 15\,\mathrm{eV/c^2}$ [Sis04]. In order to improve this limit by two orders of magnitude a project for an array of at least 10 000 calorimetric detectors was proposed – the MARE [Mar06] project.

As seen earlier the fraction of events in the region of the end-point of the spectrum is crucial and scales with $(\delta E/E_0)^3$. Therefore choosing the isotope ^{187}Re with the lowest known Q-value (2.47 keV) for a neutrino mass experiment is more than

reasonable. Compared to tritium experiments this leads to a reduction in the required count rate of about 400. At a first glance the activity of 1 Bq/mg of natural rhenium seems to be extremely low but it is perfectly suited for this type of detector as will be seen later.

The most important parameters of these experiments – the total number of events N_ν, the energy resolution ΔE and f_{pu} and the rate of time unresolved superposition of β-decays – are derived from characteristics of real detectors. The total number of events can be written as the product of the number of detectors N_{det}, the activity A for one detector and the measuring period t_{m}

$$N_\nu = N_{\mathrm{det}} A t_{\mathrm{m}}. \tag{2.10}$$

The energy resolution ΔE of the detector is taken as the FWHM[3] of a gaussian (assuming a gaussian response of the detector).

For this project a Monte Carlo code was developed, in which β-spectra are simulated. The simulated data is fitted afterwards to estimate the statistical sensitivity of a neutrino mass experiment performed with calorimeters. These simulations were done based on state of the art detectors existing today with a plausible energy resolution between 5 eV and 20 eV and a pile up rate of $f_{\mathrm{pu}} = 10^{-5}$ combined with an activity of 1 Bq. Figure 2.4 (left) shows the total number of events needed with given values for the energy resolution of each detector and a given fraction of undetected pile up events.

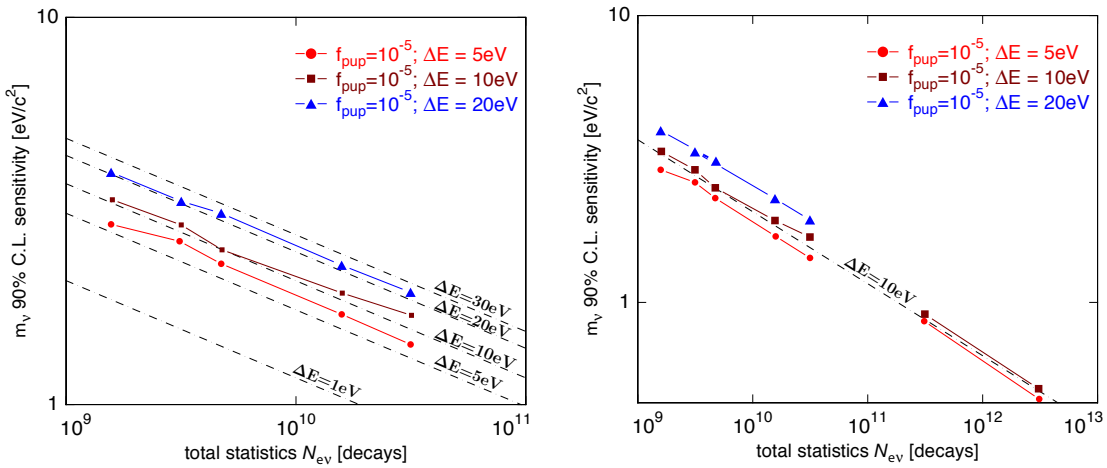

Figure 2.4 Left: Monte Carlo simulations showing 90% confidence level m_ν sensitivity as function of total number of events N_ν for different achievable experimental setups. [And07]. Right: Results from Monte Carlo simulations for large statistics [Nuc04].

The final goal of the MARE project will be the search for the neutrino mass with the same sensitivity as the KATRIN experiment of about 0.2 eV/c^2 [And07]. Also for this regime the dependence of the sensitivity on the number for detected events

[3]Full Width Half Maximum

was simulated and is shown in Figure 2.4 (right). Employing a new generation of detectors with an energy resolution of 1 eV and pile up rate of $f_{\mathrm{pu}} = 10^{-5}$ a total of 10^{14} events need to be measured to reach the planned sensitivity of KATRIN. An array of 50 000 such calorimeters with a rhenium activity of about 5 Bq would detect about $8 \cdot 10^{12}$ events a year. The simulations show that such an experiment with currently available techniques is too challenging but might be possible thanks to new developments in the field of low temperature detectors.

Since the determination of the neutrino mass or its upper limit is of major interest in today's particle physics there is an evident motivation for developing an experiment complementary to KATRIN. Based on the research that has already been done within the MARE collaboration in this thesis a prototype metallic magnetic calorimeter with a superconducting rhenium absorber is studied and presented in the following chapters.

3. Theoretical Background

3.1 Principles of Metallic Magnetic Calorimeters

In this section the underlying principles of metallic magnetic calorimeters (MMCs) will be discussed. The detection scheme is described, general requirements are addressed as well as limits on the energy resolution for this family of detectors. The basic idea behind a calorimetric measurement was already mentioned in section 2.2.2. A schematic of a MMCs is shown in Figure 3.1: the temperature is monitored based on the magnetic properties of solids. Two motivations lead to this method, one being the fact that the magnetic properties of solids are strongly dependent on temperature, the other is the existence of highly sensitive methods to read out magnetization changes.

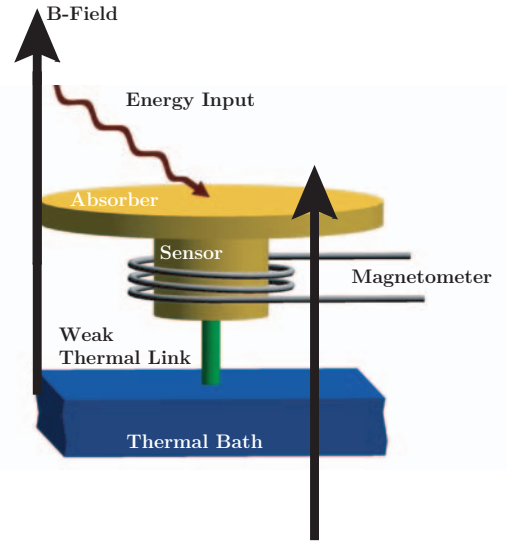

Figure 3.1 Schematic of a MMC. A sensor is placed in an external magnetic field, it is thermally weakly linked to a thermal bath. The absorption of an energetic particle increases the temperature and thus reduces the magnetization of the sensors. This change is read out by a SQUID magnetometer.

In the Eighties of the last century [Uml88] it was first proposed to use paramagnetic sensors in small magnetic fields as low temperature detectors. The magnetization of dielectric paramagnets with $4f$ ions was used. Because of the long relaxation times of spins and phonons due to their weak coupling at low temperatures in the early Nineties metallic hosts were introduced [Ban93] featuring a much faster relaxation of magnetic moments and electrons (in the order of $0.1\,\mu$s). The drawback of the presence of conduction electrons is an increase of the sensor's heat capacity and stronger interaction among the magnetic moments due to the indirect RKKY interaction[1].

The absorption of an energetic particle with the energy δE is followed by a rise in temperature δT and with this a decrease in magnetization δM of the sensor, which is read out. From equilibrium thermodynamics the change of magnetization caused

[1] Initialism for the physicists Ruderman, Kittel, Kasuya and Yosida

by the absorption of the energy can be written as

$$\delta M = \frac{\partial M}{\partial T}\,\delta T = \frac{\partial M}{\partial T}\,\frac{\delta E}{C_{\mathrm{tot}}}, \tag{3.1}$$

where C_{tot} is the total heat capacity of the calorimeter, i.e. the heat capacity of the spins and all other degrees of freedom like electrons and phonons. Considering a system of non-interacting spins with $S = 1/2$ in an external magnetic field B the magnetic moments can occupy two possible states that show a Zeeman splitting of

$$E_{\mathrm{z}} = g\mu_{\mathrm{B}}B \tag{3.2}$$

with the effective Landé factor g and the Bohr magneton $\mu_{\mathrm{B}} = 9.27 \cdot 10^{-24}\mathrm{JT}^{-1}$. For example a magnetic field of 5 mT and an effective Landé factor $g = 6.8$ leads to an energy splitting of about 2 μeV.

The deposition of the energy δE induces a change in the number of spins aligned antiparallel to the magnetic field $\delta N = \delta E/E_{\mathrm{z}}$. Evidently this is directly related to a change in magnetization

$$\delta m = \delta N g\mu_{\mathrm{B}} = \frac{\delta E}{E_{\mathrm{z}}} g\mu_{\mathrm{B}} = \frac{\delta E}{g\mu_{\mathrm{B}}B}\, g\mu_{\mathrm{B}} = \frac{\delta E}{B}. \tag{3.3}$$

If a circular loop of wire with radius r is placed around a sample of non-interacting spins the change in magnetization will create a flux change $\delta\Phi$ within the loop

$$\delta\Phi = \mu_0 \frac{G}{r}\delta m, \tag{3.4}$$

where μ_0 is the permeability of free space and G is a dimensionless factor of the order of 1 that describes the coupling of the sensor's spins to the detection loop depending on their mutual geometry.

The signal of an MMC is not based on transport properties like in resistive calorimeters, instead we measure the magnetization of a paramagnetic sensor which is an equilibrium thermodynamic property. Once the properties of the magnetic moments and the interaction among them and their surroundings is known it is possible to calculate the response to an energy input δE.

At this stage there is a thorough understanding of the employed paramagnetic alloy gold erbium, which will be presented in section 3.3. This makes further optimization of detectors more easy.

3.2 Fundamental Limits on the Energy Resolution

In a low temperature calorimeter there are several impacts on the energy resolution like for example temperature fluctuations, electromagnetic influences of the surroundings or infrared radiation due to imperfect thermal shielding. Putting all these influences aside in a metallic magnetic calorimeter there are more intrinsic contributions like the magnetic Johnson noise generated by the metallic sensor, flux noise from the SQUID or thermal fluctuations of magnetic moments.

The most fundamental limitations on the energy resolution are defined by fluctuations of energy between the subsystems of the calorimeter and by fluctuations between the calorimeter and the thermal reservoir. The situation is pictured in Figure 3.2.

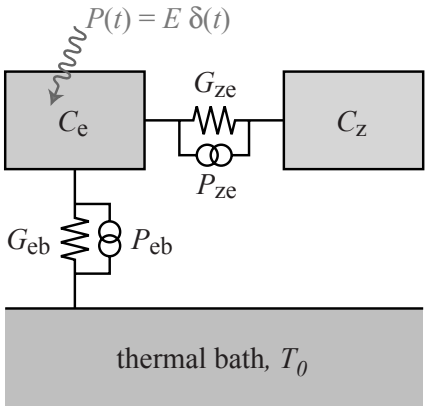

Figure 3.2 A simplified model of a magnetic calorimeter with two subsystems. The conduction electrons of the absorber and the sensor are combined to a heat capacity C_e, the magnetic moment subsystem has a heat capacity C_z.

The pictured canonical ensemble consists of two subsystems. The conduction electrons of sensor and absorber on the top left are thermally linked by the conductance G_ze to the subsystem of the spins (top right). Both systems feature the heat capacities C_e and C_z, respectively. The electronic system is furthermore connected to the thermal bath with temperature T_0 via a thermal link G_eb. We want to assume the magnetic moments to be non-interacting. The energy fluctuations causing the limitation on the energy resolution originate within the thermal couplings G_ze and G_eb. The quantities $P_\mathrm{ze} = 4k_\mathrm{B}G_\mathrm{ze}$ and $P_\mathrm{eb} = 4k_\mathrm{B}G_\mathrm{eb}$ represent randomly fluctuating fluxes of heat through the thermal links. An additional energy input δE in this model is assumed to thermalize instantaneously and is pictured as a power input $P(t) = E\,\delta(t)$. The energy content and its evolution in time can be described using differential equations (see [Fle05])

$$\begin{aligned} \dot{E}_\mathrm{z} &= C_\mathrm{z}\dot{T}_\mathrm{z} = -(T_\mathrm{z} - T_\mathrm{e})G_\mathrm{ze} + P_\mathrm{ze} \\ \dot{E}_\mathrm{e} &= C_\mathrm{e}\dot{T}_\mathrm{e} = -(T_\mathrm{e} - T_\mathrm{z})G_\mathrm{ze} - (T_\mathrm{e} - T_0)G_\mathrm{eb} + P_\mathrm{ze} + P_\mathrm{eb} + P(t). \end{aligned} \tag{3.5}$$

The spectral power density $S_{\mathrm{E_z}}$ of the energy fluctuations of the magnetic moments is given by the solution where the power input $P(t)$ is set to zero and equations (3.5) are transformed to the frequency domain

$$S_{\mathrm{E_z}}(f) = k_\mathrm{B}C_\mathrm{z}T^2\left(\alpha_0\frac{4\tau_0}{1+(2\pi\tau_0 f)^2} + \alpha_1\frac{4\tau_1}{1+(2\pi\tau_1 f)^2}\right). \tag{3.6}$$

Here τ_0 and τ_1 represent the characteristic time constants of the system. Both as well as the dimensionless factors α_0 and α_1 are somewhat cumbersome functions of C_z, C_e, G_ze and G_eb.

For heat capacities of the electron and spin systems that are of the same order of magnitude $C_\mathrm{e} \simeq C_\mathrm{z}$, and for a significantly shorter rise than fall time $\tau_0 \ll \tau_1$ one can

use the approximations $\alpha_0 \simeq (1-\beta)$ and $\alpha_1 \simeq \beta$ where β is the relative heat capacity contribution of the Zeeman system to the total heat capacity $\beta = C_z/(C_e + C_z)$.

On the other hand the response of the system to a delta like heat input can be calculated, in this case neglecting the random noise sources. Here the energy content E_z of the system will rise with a time constant τ_0 and after running through a maximum it will relax with the time constant τ_1. In frequency domain the signal shape is given by

$$|p(f)| \simeq \frac{2\beta\tau_1}{\sqrt{1+(2\pi\tau_0 f)^2}\sqrt{1+(2\pi\tau_1 f)^2}}. \tag{3.7}$$

For typical parameters ($C_z = 5\,\mathrm{pJK^{-1}}$, $C_e = 1\,\mathrm{pJK^{-1}}$, $T = 50\,\mathrm{mK}$, $\tau_0 = 5\,\mu\mathrm{s}$ and $\tau_1 = 5\,\mathrm{ms}$) the spectral power densities of the energy fluctuations and of the response of the same detector are shown in Figure 3.3.

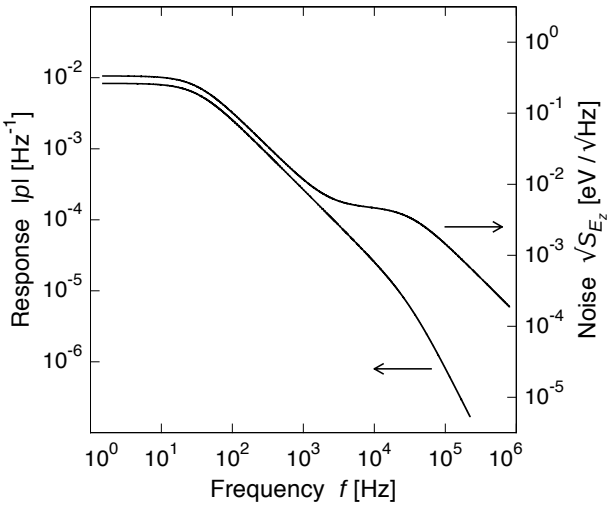

Figure 3.3 The spectral power density $\sqrt{S}$ of the energy fluctuations (right axis) and of the response to a delta like heat input (left axis).

The frequency spectrum of the energy fluctuations is an incoherent sum of two contributions, each thermal link showing up as a step like plateau. At high frequencies the fluctuations between spins and absorber electrons appear with an amplitude of $\sqrt{S_{E_z}} = \sqrt{4k_B C_z T^2 \tau_0 (1-\beta)}$, at frequencies below $f_1 = (2\pi\tau_1)^{-1}$ the other link represented by G_{ze} is dominant with an amplitude of $\sqrt{S_{e_z}} = \sqrt{4k_B C_z T^2 \tau_1 \beta}$.

The power spectrum of a detector response can be divided into three frequency domains. There is a constant regime for frequencies lower than $f_1 = (2\pi\tau_1)^{-1}$, above this frequency the amplitude is decreasing with f^{-1} and for frequencies higher than $f_0 = (2\pi\tau_0)^{-1}$ the amplitude decreases proportionally to f^{-2}.

Assuming an algorithm based on the concepts of optimal filtering to derive the signal height in the presence of noise it is possible to calculate a fundamental limitation to the energy resolution [McC05] from the ratio of the calculated signal and

noise $SNR(f) = |p(f)|^2/S_{\mathrm{E_z}}$. For the present case this results in

$$\Delta E_{\mathrm{rms}} = \left(\int_0^\infty SNR^2(f) df \right)^{-1/2} = \sqrt{4k_{\mathrm{B}}C_{\mathrm{e}}T^2} \left[\frac{G_{\mathrm{eb}}}{G_{\mathrm{ze}}} + \left(\frac{G_{\mathrm{eb}}}{G_{\mathrm{ze}}} \right)^2 \right]^{\frac{1}{4}}. \tag{3.8}$$

The energy resolution is proportional to the energy fluctuations of a canonical ensemble $\sqrt{k_{\mathrm{B}}C_{\mathrm{e}}T^2}$. Expression (3.8) shows that the energy resolution in theory can be increased without limits by improving the thermal conductance G_{ze} between the electronic and Zeeman-system. In terms of relaxation times (3.8) can be rewritten as

$$\Delta E_{\mathrm{rms}} = \sqrt{4k_{\mathrm{B}}C_{\mathrm{e}}T^2} \left(\frac{1}{\beta(1-\beta)} \right)^{\frac{1}{4}} \left(\frac{\tau_0}{\tau_1} \right)^{\frac{1}{4}}. \tag{3.9}$$

In reality the material specific electron-spin relaxation time τ_{K} that obeys the Korringa relation $\tau_{\mathrm{K}}T = \kappa$ will be a limiting factor for the rise time τ_0. Furthermore, in this formulation it can be seen that the energy resolution will benefit from long decay times τ_1, meaning a weak link to the the thermal bath. However one needs to bear in mind that long decay times also imply low achievable count rates.

To illustrate the discussed limitation on the energy resolution, two plausible detectors are assumed to have $C_{\mathrm{e}} = 1\,\mathrm{pJK^{-1}}$, $C_{\mathrm{z}} = 5\,\mathrm{pJK^{-1}}$, $\tau_0 = 5\,\mu\mathrm{s}$ (or $\tau_0 = 500\,\mu\mathrm{s}$) and $\tau_1 = 5\,\mathrm{ms}$. Featuring a working temperature of about 50 mK this results in a $\Delta E_{\mathrm{rms}} \simeq 0.7\,\mathrm{eV}$ or $\Delta E_{\mathrm{rms}} \simeq 2.2\,\mathrm{eV}$ respectively.

The fundamental energy resolution found here proves to be low enough to be in line with the requirements of direct neutrino mass measurements. Other sources of noise limiting the energy resolution will be discussed in sections 3.6 and 4.2.3.

3.3 Sensor Material

The choice of a suitable material for the paramagnetic sensor is crucial. The historic development towards a metallic host material was mentioned before. In this section the employed alloy of gold (Au) with a dilute concentration of the rare earth metal erbium (Er) is discussed in some detail.

3.3.1 Basic Properties of Au:Er

In low concentrations erbium forms a solid solution with gold [Rid65]. Er^{3+} ions substitute for Au at regular sites in the fcc matrix. The electron configuration of the Er^{3+} is given as $[Kr]4d^{10}4f^{11}5s^25p^6$. The electrons of the just partially filled $4f$ shell carry a permanent magnetic moment and thus give rise to the paramagnetic behavior. With a radius of just about 0.3 Å the $4f$ shell is located deep inside the outer $5s$ and $5p$ shells greatly reducing the influence of the crystal field. Therefore the magnetic moment can be calculated from the orbital angular momentum $\boldsymbol{L}$, the

spin angular momentum $\boldsymbol{S}$ and the resulting total angular momentum $\boldsymbol{J}$ according to Hund's rules. This at least holds for temperatures higher than 100 K. Below this, the crystal field splits the sixteen fold degeneracy of Er^{3+} into a series of multiplets, the lowest in energy being a Γ_7-Kramers doublet. The zero field energy splitting between the Kramers doublet and the in energy next higher Γ_8 quartet has been found to be between $\Delta E = 11\,\mathrm{K} \cdot k_\mathrm{B}$ and $\Delta E = 19\,\mathrm{K} \cdot k_\mathrm{B}$ [Wil69, Sjo75, Dav73, Hah92]. Probably the most reliable value obtained by neutron scattering can be regarded to be $\Delta E = 17\,\mathrm{K} \cdot k_\mathrm{B}$ [Hah92]. For weak fields and sufficiently low temperatures this justifies an approximation for the behavior of erbium in gold as a two level system with a quasi spin[2] $S = 1/2$ and an effective isotropic Landé factor of $g = 34/5$ [Abr70].

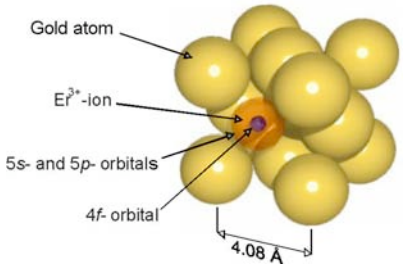

Figure 3.4 Schematic depiction of a Au lattice unit cell where one Au^+ ion is replaced by Er^{3+}. The Er^{3+} ions are found at regular lattice sites of the gold fcc lattice.

Contrary to other calorimetric detection concepts for the presented detectors the thermodynamic equilibrium property magnetization is used as a thermometer. This is determined by the equilibrium thermodynamic properties of the sensor material which will be described in the following section.

3.3.2 Heat Capacity and Magnetization

The heat capacity and the magnetization of Au:Er will determine the performance of a magnetic calorimeter. In this section the most important thermodynamic properties of Au:Er are presented and discussed (for a more detailed discussion see [Fle05]). The MMC will be operated at low temperatures between 30 mK and 100 mK, therefore just the ground state doublet mentioned before is considered in the calculations.

A first approach to the study of Au:Er will be the consideration of a system of non-interacting spins in a homogenous magnetic field. To describe the thermodynamic system of N magnetic moments each occupying one of the two possible eigenstates, separated by the energy $E = g\mu_\mathrm{B}B$, one can choose the thermodynamic potential free energy. The heat capacity of such a system can be described by the well known Schottky expression

$$C_\mathrm{z} = Nk_\mathrm{B}\left(\frac{E}{k_\mathrm{B}T}\right)^2 \frac{\mathrm{e}^{E/k_\mathrm{B}T}}{(\mathrm{e}^{E/k_\mathrm{B}T}+1)^2}. \tag{3.10}$$

As can be seen in Figure 3.5 the heat capacity exhibits a maximum when the thermal energy $k_\mathrm{B}T$ is about half the energy splitting.

[2] It is important to note that this is not a genuine spin 1/2 system. For temperatures far below the splitting energy it is still justified to only consider the lowest energy doublet of the energy scheme. This quasi spin $\tilde{S}$ will be denoted as S within this work.

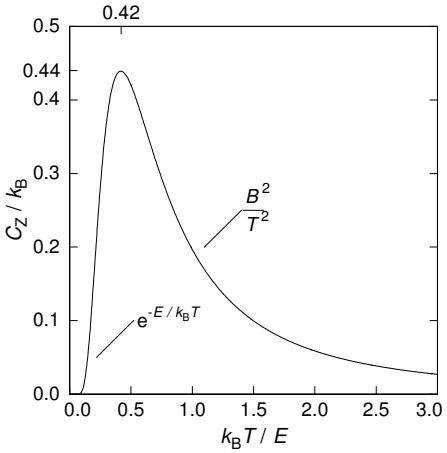

Figure 3.5 Heat capacity of a two level system as a function of the reduced temperature k_BT/E. E denotes the energy splitting $E = g\mu_B B$ of the Zeeman system. Approximations for high and low temperatures are also given.

For $S = 1/2$ the magnetization of such a system can be calculated to be

$$M = \frac{N}{V} g S \mu_B \mathcal{B}_S(h) = \frac{N}{V} \frac{1}{2} g \mu_B \tanh\left(\frac{g\mu_B B}{2k_B T}\right) \tag{3.11}$$

with the spin S, the Landé factor g and $h = \frac{Sg\mu_B B}{k_B T}$ as the argument of the so called the Brillouin function. For $S = 1/2$ the Brillouin function simplifies to $\mathcal{B}_{1/2}(h) = \tanh(h)$. For high temperatures ($h \ll 1$) the magnetization shows a Curie behavior as expected for a paramagnetic substance as shown in Figure 3.6. For low temperatures ($h \gg 1$) the magnetization reaches a point of saturation thus the Brillouin function deviates strongly from the Curie behavior.

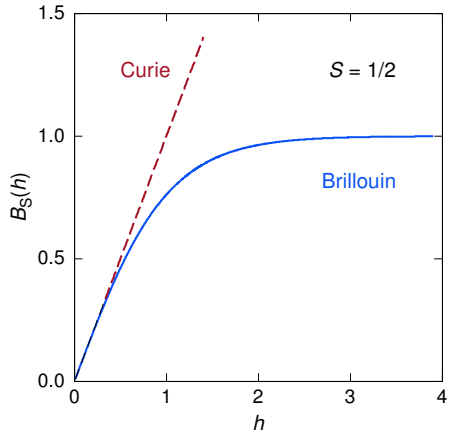

Figure 3.6 Brillouin function $\mathcal{B}_{1/2}(h) = \tanh(h)$ for $S = 1/2$. For high temperatures a Curie approximation is displayed.

The previously used assumptions of non-interacting magnetic moments within an applied external field is sufficient for a qualitative description of the sensor material but not for a quantitative analysis. To calculate the response of a MMC the magnetic dipole-dipole interaction as well as the indirect RKKY exchange coupling need to be included. Different methods have been used to calculate the required thermodynamic quantities, the magnetization and the heat capacity. Both a mean-field approach [Hor99] and a method using the numerical diagonalization of a Hamiltonian including both mentioned interactions were used for the understanding of the sensor material

Au:Er. The results of the second method [Sch00, Fle03] will be used within this work.
In Figure 3.7 (left) the magnetization M of a Au:Er sensor is plotted for different magnetic fields B ranging from 0.87 mT to 12.8 mT versus the inverse temperature. Also the specific heat as a function of temperature is shown for different fields in a similar range. The erbium concentration of the sample in these measurements is 300 ppm. Numerically calculated data is depicted as solid lines, whereas points represent measured data. In order to develop a feeling for the recurrent magnitude of specific heat, the electronic and the phononic contribution to the specific heat in gold are shown in the figure as well.

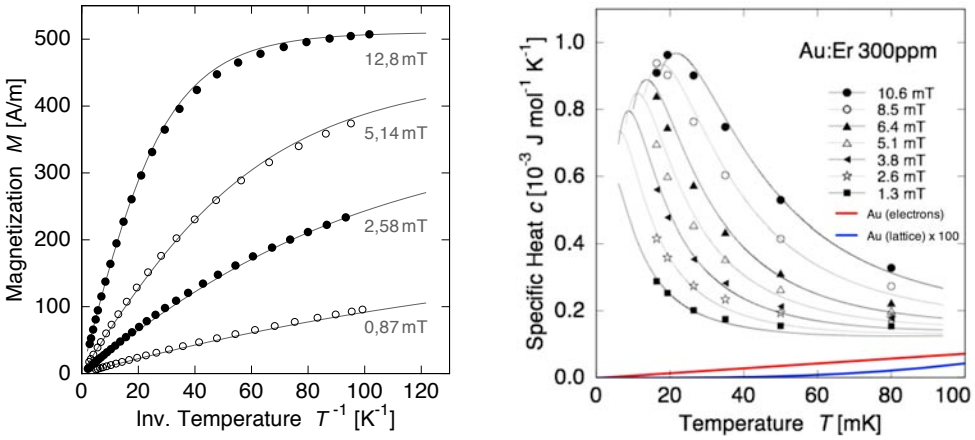

Figure 3.7 The left hand plot shows the magnetization of Au:Er with a concentration of 300 ppm erbium as a function of inverse temperature at various applied magnetic fields. The right hand plot shows the specific heat for the same Au:Er sample. For both plots the solid lines represent results of the numerical calculations and the points represent measured data [Fle05]. For the specific heat also contributions of the electrons (red line) and phonons (blue line) in gold are given. Note that the phonon contribution has been multiplied by a factor of 100 to appear in the same range.

In high magnetic fields and for low temperatures the magnetization shows the expected saturation. Including the interaction the maximum value is decreased by about 10 %. The impact of the interaction on the magnetization can be observed by looking at the data that was measured in the small magnetic field $B = 0.87$mT If the high temperature behavior is linearly extrapolated to low temperatures the magnetization shows to be reduced up to 30% for the lowest temperatures.

The heat capacity shows a Schottky anomaly, as expected. The temperature of the specific heat maximum is dependent on the strength of the magnetic field. However, the width of the maximum is about twice the size compared to a non-interacting spin system. Altogether the model seem to describe the situation in a satisfactory manner such that the thermodynamic properties of the sensor material Au:Er can be considered as understood. These numerically calculated data will be used to discuss the properties of the magnetic calorimeter to read out the rhenium absorber and thus will be of major importance.

3.3.3 Detector Signal

The energy absorption in a detector is followed by a change in magnetic moment δm of the sensor with volume V

$$\delta m = V \delta M. \tag{3.12}$$

Assuming that just the non-interacting spin system determines the thermodynamic properties, this system is solely able to absorb energy by flipping individual spins. Each of those spin flips requires the splitting energy $E = g\mu_\mathrm{B}B$ and changes the total magnetic moment of the sensor by $g\mu_\mathrm{B}$, the signal size will be given by

$$\delta m = g\mu_\mathrm{B}\frac{\delta E}{g\mu_\mathrm{B}B} = \frac{\delta E}{B}. \tag{3.13}$$

With this simplification the signal size increases proportionally to $1/B$ as the Zeeman splitting is reduced with smaller fields.

In reality in a magnetic calorimeter there is more than just the thermodynamic spin system to be considered, for example the systems of the conduction electrons and the lattice. Here it is important to recall that a detector mostly consists of a sensor and an absorber such that all of those heat capacities need to be considered. Calculating the heat capacity of the electrons and the lattice of gold at a temperature of $T = 50\,\mathrm{mK}$ reveals that the phononic contribution is negligible but the electrons need to be considered. The specific heat of the electron system in gold is described by $C_\mathrm{e} = \gamma T$, with $\gamma = 7.29\,10^{-4}\mathrm{Jmol}^{-1}\mathrm{K}^{-2}$ [Kit06]. The specific heat of the phonon system is given by $C_\mathrm{ph} = \beta T^3$, with $\beta = 4.4\,10^{-4}\mathrm{Jmol}^{-1}\mathrm{K}^{-4}$ [Kit06] and thus is negligible for the temperature range under investigation.

The electron-spin interaction in paramagnetic metals is very strong and therefore it leads to relaxation times in the microsecond range even at temperatures below 50 mK. This means that energy deposited in either system will be shared rapidly among both. Taking this into account just a fraction δE_z of the deposited energy δE will flow into the spin system causing a change in magnetization and thus gives rise to a signal

$$\delta E_\mathrm{z} = \frac{C_\mathrm{z}}{C_\mathrm{z} + C_\mathrm{e}}\delta E, \tag{3.14}$$

where C_z and C_e are the heat capacities of the Zeeman system and the conduction electrons respectively.

Including the heat capacity of the electrons of sensor and absorber in the model the behavior of the detector signal changes fundamentally. Figure 3.8 shows the change of the sensor's magnetic moment caused by the absorption of a 5.9 keV X-ray displayed as a function of magnetic field B for two possible working temperatures. This was calculated assuming a non-interacting spin-1/2 system and including the electronic heat capacities of a detector consisting of a sensor and an absorber, both are assumed to be foils with the size of $200 \times 200 \times 5\,\mu\mathrm{m}^3$.

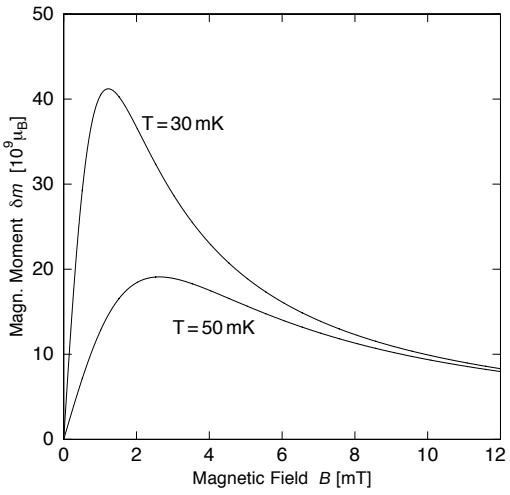

Figure 3.8 Change in the magnetic moment δm after the absorption of $E = 5.9\,\mathrm{keV}$ in a detector as a function of the magnetic field B at temperatures of 30 mK and 50 mK. δm is given in units of Bohr's magnetons μ_B. For $g = 6.8$ the absorption of 5.9 keV leads to $\approx 10^{10}$ individual spin flips. The detector is assumed to consist of a Au:Er sensor with an erbium concentration of 600 ppm and a gold absorber of the same dimensions ($200 \times 200 \times 5\,\mu\mathrm{m}^3$).

The overall behavior can be understood with what has been discussed before. For small magnetic fields $g\mu_\mathrm{B}B \ll k_\mathrm{B}T$ the heat capacity of the Zeeman system will rise proportionally to $C_\mathrm{z} \propto B^2$. Combining this with (3.13) the total change in magnetic moment will show a behavior $\delta m \propto B$. In the limit for large magnetic fields $g\mu_\mathrm{B}B \gg k_\mathrm{B}T$ the heat capacity of the spin system is dominant and the part of the energy going into the Zeeman system is nearly field independent ($\delta E_\mathrm{z} \simeq \delta E$). Still the Zeeman splitting is increased with higher fields, so less spins flip with the same amount of energy deposited, leading to a δm inversely proportional to B. For medium sized fields the signal size will feature a maximum as seen in Figure 3.8. Both, the height and the width of the maximum depend on the working temperature of the MMC. As a rough rule of thumb the maximal signal size will be obtained in a magnetic field B_max where the heat capacity of the spin system equals the heat capacity of all other systems within the detector $C_\mathrm{z}(B_\mathrm{max}, T) = C_\mathrm{e}(T)$.

3.3.4 Influence of Nuclear Spins

So far erbium was discussed as carrying no nuclear spin which is true for all but one isotope: ^{167}Er with $I = 7/2$ occurring naturally with an abundance of 23%. The presence of this nuclear moment will effect the magnetization and heat capacity due to its hyperfine interaction with the $4f$-shell electrons. The level scheme of the Kramers-Γ_7 doublet of ^{167}Er is shown in Figure 3.9. Compared to erbium without nuclear spin discussed before this scheme cannot be simplified as easily, the system cannot be treated as a two level system anymore. For zero magnetic field the level scheme is divided into two groups which are separated by a gap of $E = 140\,\mathrm{mK} \cdot k_\mathrm{B}$. The groups can be characterized by their total angular momentum $F = 3$ (7 eigenstates) and $F = 4$ (9 eigenstates).

This fact is reflected in a considerable difference in magnetization and heat capacity compared to what was discussed before. In the temperature and magnetic field range of interest the magnetization is reduced, simultaneously the heat capacity is enhanced. The specific heat of a Au:Er sample with natural isotope abundance

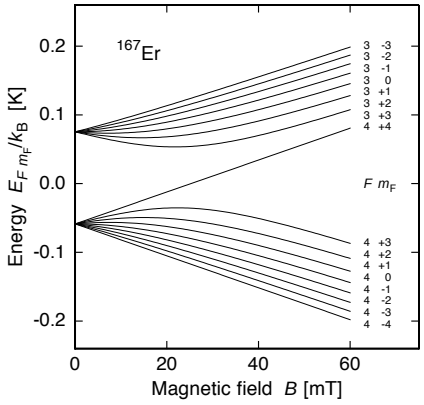

Figure 3.9 The plot shows the hyperfine splitting of the Kramers-Γ_7 doublet of ^{167}Er as a function of the applied magnetic field. It is divided into two groups with total angular momenta $F = 3$ and $F = 4$ and has a zero field energy splitting of about $140\,\mathrm{mK} \cdot k_\mathrm{B}$. For small fields the gap between two adjacent energy levels increases linearly with the magnetic field [Fle03].

is shown in Figure 3.10. For weak magnetic fields there are two maxima. The first at lower temperatures is caused by excitations of spins within the $F = 4$ multiplet and by contributions of erbium ions of the other isotopes as discussed before. This maximum is strongly dependent on the magnetic field.

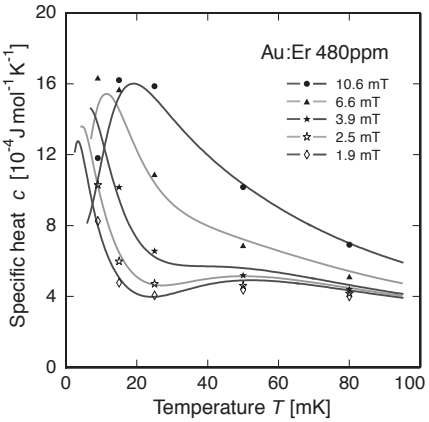

Figure 3.10 The specific heat of Au:Er with a concentration of 480 ppm natural erbium [Fle00] as a function of temperature for different magnetic fields. Two maxima can be observed, one strongly field dependent maximum at low temperatures and one at higher temperatures caused by ^{167}Er. Measured data is depicted as points.

For higher temperatures there is another broad maximum in the specific heat which is nearly independent of magnetic field. The maximum is caused by excitations from energy levels of the lower $F = 4$ eigenstates to those of the energetically higher $F = 3$ eigenstates. For ^{167}Er these transitions are not necessarily followed by a change in magnetization, meaning energy can be absorbed by the Zeeman system of the ^{167}Er without a resulting signal. In weak magnetic fields and at temperatures around 50 mK this contribution dominates the specific heat. For the highest sensitivity erbium depleted of the isotope 167 should be used.

In the presented work two types of erbium diluted in gold were used. Au:Er foils with enriched erbium with only a concentration of 2.8% of the isotope ^{167}Er. Secondly sputtered films were produced with a Au:Er sputter target containing erbium in the natural isotope abundance.

3.4 Physical Properties of Rhenium

After presenting properties of the sensor material now the absorber material rhenium will be discussed. Some general properties are displayed in Table 3.1.

Atomic number	75
Natural abundance	^{185}Re (37.4%), ^{187}Re (62.6%)
Half life of ^{187}Re	43.2 Gy
Molar mass M_{mol}	$186\,\mathrm{g\,mol^{-1}}$
Density	$21.02\,\mathrm{g\,cm^{-3}}$
Electronic configuration	$[Xe]4f^{14}5d^{5}6s^{2}$
Crystal structure	hcp
Debye temperature Θ_{D}	417 K
Transition temperature T_{c}	1.69 K
Melting point	3459 K
Critical field B_{C} at $T = 0\,\mathrm{K}$	20.0 mT
El. resistivity (300 K)	$18\,\mu\Omega$cm

Table 3.1 Some general properties of rhenium at a glance [Win07, Kit06, Sis04].

The rare transition metal rhenium naturally occurs as a mix of ^{185}Re, which is stable, and ^{187}Re, which is unstable. Rhenium crystals have a hexagonal close-packed structures and are type I superconductors below $T_{\mathrm{c}} = 1.7\,\mathrm{K}$. Their melting point of more than 3400 K and density of $21.02\,\mathrm{g\,cm^{-3}}$ are only exceeded by a few elements.

3.4.1 β-decay of ^{187}Re

In the experiments discussed here rhenium is not just supposed to serve as an absorber for energetic photons but also to serve as a source for the electrons emitted by the β-decay of ^{187}Re. This isotope is unstable with a comparably long lifetime of about $\tau_{1/2} = 43.2$Gy [Sis04] and decays by a single unique, first forbidden transition to the ^{187}Os ground state

$$^{187}\mathrm{Re} \rightarrow {}^{187}\mathrm{Os} + \mathrm{e}^{-} + \overline{\nu_{\mathrm{e}}} \tag{3.15}$$

Considering the long half life of ^{187}Re, the natural isotope abundance c_{187} and the molar mass M_{mol} the activity A is given by

$$A = c_{187}\frac{m_{\mathrm{Re}}N_A}{M_{\mathrm{mol}}}\frac{1}{\tau_{1/2}}. \tag{3.16}$$

For 1 mg of rhenium this gives an activity of about 1.4 Bq. As discussed in section 2.2.2 in respect to pile-up events the total activity is a crucial parameter for calorimetric measurements of the neutrino mass. The given activity of a detector with bulk rhenium of that weight does indeed suite the needs for those experiments [Raz03]. A rhenium absorber of 1 mg would for example be a cuboid with side lengths $250 \times 250 \times 750\,\mu\mathrm{m}^3$.

3.4.2 Heat Capacity

The heat capacity of rhenium has been studied by various groups [Sha67, GHa71] and two regimes need to be discussed separately: firstly rhenium in the normal conducting phase and then evidently, for the present purpose, rhenium at temperatures below T_c – in the superconducting state.

Normal Conducting Regime

In the temperature range above the transition to superconductivity the heat capacity of rhenium can be written as [GHa71]

$$C = AT^{-2} + BT^{-3} + \gamma T + \beta T^3 \tag{3.17}$$

with $A = 40.6\,\mu\text{Jmol}^{-1}\text{K}$, $B = 0.0034\,\mu\text{Jmol}^{-1}\text{K}^2$, $\gamma = 2290\,\mu\text{Jmol}^{-1}\text{K}^{-2}$ and $\beta = 27\,\mu\text{Jmol}^{-1}\text{K}^{-4}$. The first two terms represent the quadrupole contribution of the nuclei and the last two are the electronic and lattice contributions. For a temperature of 50 mK the heat capacity of 1 mg of rhenium adds up to $C = C_n + C_{e,nc} + C_l = 17486\,\text{pJK}^{-1} + 615\,\text{pJK}^{-1} + 0.018\,\text{pJK}^{-1} = 18101\,\text{pJK}^{-1}$. Rhenium shows a very large nuclear heat capacity and also the electronic heat capacity is three times larger than for gold. Therefore it would not be suited as a normal conducting absorber for a calorimeter.

Superconducting Regime

Below its critical temperature the heat capacity of rhenium shows a different behavior. On the one hand the spin-lattice relaxation times become very long (presumably on the order of tens of seconds like in other superconductors [Phi64]), thermally isolating the nuclear spin system. So for temperatures below T_c on the time scale of the transient signals upon particle detection no nuclear heat capacity is expected to be observed. On the other hand the electrons will form Cooper pairs and, as a result, also the electronic contribution to the heat capacity will diminish. The properties of superconducting rhenium are in agreement with the properties of a weak-coupling superconductor calculated on the basis of the BCS theory of superconductivity. The electronic contribution to the heat capacity in the superconducting state well below the transition temperature can be expressed as

$$C_{e,sc} = a\gamma T_C \exp\left(-bT_C/T\right) \tag{3.18}$$

with $a = 8.14$, $b = 1.413$ and $\gamma = 2290\,\mu\text{Jmol}^{-1}\text{K}^{-2}$ [Smi70]. The contributions to the heat capacity of the lattice and the electrons at 50 mK will now sum up to $C = C_{e,sc} + C_l = 410^{-12}\,\text{pJK}^{-1} + 0.02\,\text{pJK}^{-1} = 0.02\,\text{pJK}^{-1}$, a value nearly six orders of magnitude below that of the normal conducting state.

These considerations emphasize the importance of rhenium becoming superconducting at the detector's working temperatures. The extremely low heat capacities of superconducting absorbers with comparably large volumes make these materials

of general interest for calorimetric detectors. Still superconducting absorbers are not widely used yet, mainly because microscopic calculations based on the BCS theory predict that a large fraction of the energy deposited in the superconductor will be stored in quasiparticle states with a long lifetime. Some aspects of the down-conversion of incoming energy in a superconductor will be discussed in the next section.

3.4.3 Energy Absorption in a Superconductor

A detailed discussion of the energy down-conversion in a superconductor is given in [Koz00, Koz00b] and references therein. In the initial phase, after the absorption of an energetic photon, a fast photoelectron is created. This electron looses its energy via secondary ionization and plasmon emission. Typically within a few femtoseconds the energy is converted into the energy of an excited hot electron-hole plasma existing in a small volume. At this point electron-electron interaction reduces the characteristic energy of the plasma. After a cross over energy the hot electrons loose energy via cascades (tens of steps) in which high frequency phonons are emitted. The emitted phonons have a long lifetime compared to the duration of the cascade. The final stage of this phase is a phonon bubble in which most of the energy is accumulated and energetic electrons with an energy below the Debye energy. This is seen as the initial distribution for a non-equilibrium system of interacting quasiparticles and phonons. A model discussing the further development of such a system is proposed in [Kap76]. The expected times for the recombination of quasiparticles with energies just above the gap edge are strongly increasing with decreasing temperature (see Figure 3.11). Already for temperatures below 100 mK the recombination times are of the order of seconds, meaning that part of the energy would be stored in the meta stable quasiparticle states and consequently would lead to a loss in the signalsize. In the figure also the scattering time of quasiparticles is depicted. This thermalization time also increases with decreasing temperature but stays in the millisecond range also for temperatures below 100 mK. In contrast to these predictions

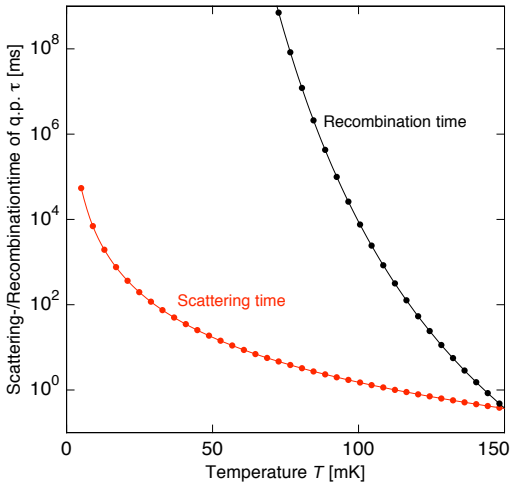

Figure 3.11 Scattering- and recombination times for quasiparticles at the gap edge of superconducting aluminum as a function of temperature (after [Kap76]).

experimental data show a different behavior. Consulich *et al.*[Con93] observed a reasonable thermalization behavior in different superconducting absorbers at least down to temperatures of $T > 2 \cdot 10^{-4}\Theta_D$. Also in a recent work with a superconducting rhenium absorber [Hau06] no irreversible deposition of energy in a system of the superconducting absorber could be observed.
Up to date there is no complete physical model or explanation for the energy down-conversion in a superconductor but the results so far definitely encourage further study of both: the measurement of the rhenium endpoint energy in respect to an upper neutrino mass limit as well as the behavior of superconducting absorbers in general.

3.5 Detector Geometry

So far the detector signal was discussed as a change of the magnetic moment δm of the entire sensor. However, the actual signal size $\delta\Phi/\delta E$ in form of the change in magnetic flux per unit of energy deposited will not solely depend on the thermodynamic properties of the absorber and sensor but also strongly on its geometry. The often used concept of a magnetic calorimeter with a pickup geometry in form of a small circular loop [Lin07] is not suited for a detector with a superconducting rhenium absorber because the magnetic field at the superconductor would be too large.

With the approach of a meander shaped pickup loop large area detectors are feasible. A cross sectional view of such a geometry is depicted in Figure 3.12. Niobium stripes of width w with a center to center distance p are located on a substrate (mostly silicon). The individual niobium stripes are connected to the adjacent stripes and form a closed loop. The niobium structure is almost completely anodized and additionally covered by a protecting SiO_2 layer. The necessary magnetic field is generated by injecting a current into the superconducting meander structure.

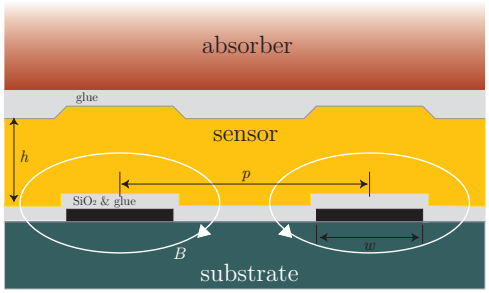

Figure 3.12 Cross-section of a meander shaped detection loop. A sensor of height h is glued on top of the meander structure followed by an absorber.

Since the spins are close to the detection loop a good sensitivity is achievable. A further benefit is the exponential decay of the magnetic field with distance z from the meander. A cross sectional view of two meander stripes can be seen in Figure 3.12. A field generating current is injected into the meander stripes of width w. This niobium structure is covered by a protecting SiO_2 layer. A sensor can be glued on this and further layers like a spacer or an absorber can be added on top. In the

following the geometry of the detector setup is linked to the measurable signal and the meander geometry used in this work is discussed in further detail.

3.5.1 Meander Geometry

The discussion here is restricted to a design in which the magnetic field is produced by passing a current through the same meander pattern that is used to measure the change in magnetization of the sensor upon the deposition of energy. Two possible realizations are shown in Figure 3.13.

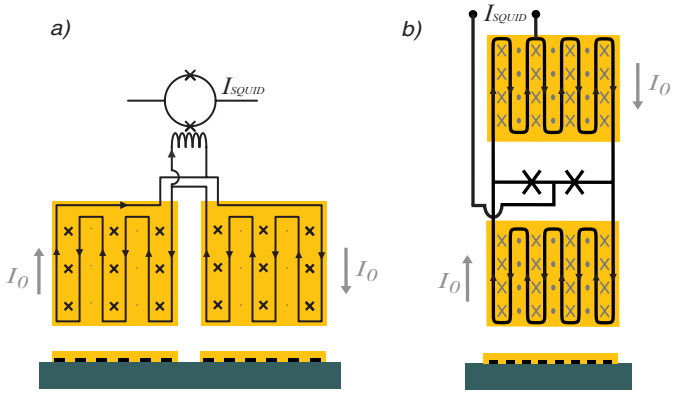

Figure 3.13 Two possible readout schemes of a meander shaped magnetic calorimeter. A persistent current I_0 in the superconducting structure produces a magnetic field. The same structure serves as pickup coil for flux changes. In a) this is transformer coupled to a SQUID. In b) the SQUID is integrated in the structure itself.

The measurable signal of a magnetic calorimeter is the change of flux $\delta\Phi$ within the area enclosed by the meander structure. This signal evidently depends on the change of the magnetic moments of the sensor but it will also depend on the geometric coupling of these to the pickup loop. In the case of a meander both the coupling and the change in magnetization will depend on their location relative to the meander. The change of flux $\mathrm{d}(\delta\Phi)$ within the meander due to a change in magnetic moment $\delta M(\boldsymbol{r})\mathrm{d}^3\boldsymbol{r}$ in the volume element $\mathrm{d}^3\boldsymbol{r}$ at the position $\boldsymbol{r}$ is given by

$$\mathrm{d}(\delta\Phi) = \mu_0 \frac{G(\boldsymbol{r}/p)}{p} \delta M(\boldsymbol{r})\mathrm{d}^3\boldsymbol{r}, \tag{3.19}$$

where $G(\boldsymbol{r}/p)$ is the dimensionless geometrical coupling factor. A simple relation between the geometric factor $G(\boldsymbol{r}/p)$, the magnetic field at the position $\boldsymbol{r}$ and the current I_0 in the meander has been shown to be [Bur04]

$$B(\boldsymbol{r}) = \mu_0 G(\boldsymbol{r}/p) \frac{I_0}{p}. \tag{3.20}$$

The deposition of the energy δE in the calorimeter will cause a change of flux $\delta\Phi$ which can be obtained by substituting (3.1) and (3.20) into (3.19) and subsequently integrating over the volume of the sensor

$$\delta\Phi = \frac{\delta E}{C_{\mathrm{abs}} + \int_V c_{\mathrm{s}}(\boldsymbol{r})\mathrm{d}^3 r} \mu_0 \int_V \frac{G(\boldsymbol{r}/p)}{p} \frac{\partial M[B(\boldsymbol{r},T)]}{\partial T} \mathrm{d}^3 r. \tag{3.21}$$

In the simpler case of a homogenous field an equally distributed change in magnetization would be expected. For a circular detection loop the geometric coupling is mainly dependent on the ratio of sensor height to the radius of the detection loop. Determining this expression in case of a meander setup is much more demanding. However it is possible to replace the integration above with an integration over G. Defining the weighted average over ζ of a quantity A as

$$\langle A \rangle_\zeta = \int P(\zeta) A \mathrm{d}\zeta, \tag{3.22}$$

it is possible to express (3.21) as

$$\frac{\delta\Phi}{\delta E} = \frac{V}{C_{\mathrm{abs}} + V \langle c_{\mathrm{s}} \rangle_{\mathrm{G}}} \mu_0 \left\langle \frac{G}{p} \frac{\partial M}{\partial T} \right\rangle_{\mathrm{G}}. \tag{3.23}$$

3.5.2 Sensitivity and Optimization

The quantity that should be maximized is not the signal size itself but rather the ratio of the size of the signal to that of the noise. The sensitivity $\mathcal{S}$ will be defined as

$$\mathcal{S} = \frac{\delta\Phi/\delta E}{\sqrt{S_\Phi}}, \tag{3.24}$$

and is to be optimized. As will be seen in section 4.2.3 a main noise contribution will be due to the SQUID magnetometer. This flux noise that is usually referred to the sensor loop will show to be proportional to the square root of its inductance, $\sqrt{S_\Phi} \propto \sqrt{L_S}$. Neglecting finite size effects the inductance of a meander shaped detection loop can be written as

$$L = \ell \mu_0 \frac{A}{p}, \tag{3.25}$$

where A is the area and p is the pitch of the meander. The dimensionless parameter ℓ is dependent on the width to pitch ratio w/p and can be determined with finite element simulations [Fle05]. For $w/p = 4/5 = 0.8$ this parameter is $\ell = 0.175$. Using (3.25) for the inductance, the sensitivity expressed in (3.24) becomes

$$\mathcal{S} = \sqrt{\frac{\mu_0}{\ell} \frac{h}{p}} \frac{\sqrt{V}}{C_{\mathrm{abs}} + V \langle c_{\mathrm{s}} \rangle_{\mathrm{G}}} \left\langle G \frac{\partial M}{\partial T} \right\rangle_{\mathrm{G}}. \tag{3.26}$$

For a calorimeter employing a meander geometry the sensitivity is a function of nine parameters

$$\mathcal{S} = \mathcal{S}(C_{\mathrm{a}}, g, \alpha, T, x, I, A, \xi, w/p). \tag{3.27}$$

Four of those, the heat capacity of the absorber C_{a}, the g-factor of the paramagnetic ions the strength of the RKKY interaction α and the working temperature T of the

detector are generally fixed by the choice of the sensor material and the experimental conditions given by the application. Furthermore, the concentration of ions x, the area A of the meander and the current flowing in the meander I influence the sensitivity as well as the ratio of the sensor height to the pitch $\xi = h/p$ and the ratio of width to pitch of the niobium structure w/p. Numerical calculations for optimizations have been made [Fle05].

Since for this work a meander structure with a certain geometry was available the area, width, and pitch were fixed. Also the current in the meander is constrained by the critical current of the niobium structure $I < I_c$ not leaving many parameters to be optimized. The free parameters of ion concentration x and reduced sensor height ξ were chosen close to the maximal signalsize, which in the present case where the noise is limited by the inductance will also be the maximum signal to noise ratio achievable. For this reason the optimization is not discussed in further detail at this point. It is still possible to show that the employed geometry is by far not optimized for the purpose, by optimizing the design the sensitivity could be improved by about one order of magnitude.

3.5.3 Magnetic Field Distribution

A discussion of the expected signal size of a detector must start with examining how the highly inhomogeneous magnetic field is distributed within the sensor. Assuming a setup as shown in Figure 3.13b two pickup coils are connected together to form a superconducting circuit, a large persistent current I_0 can be injected in it. The magnetic field produced by this current has a distribution that can be calculated numerically using the finite element program FEMM[3].

To comprehensively describe the meander three parameters have to be defined: the meander stripe width w, the pitch p and the thickness of the niobium structure. In the present case the width and pitch of the geometry are $w = 20\,\mu$m and $p = 25\,\mu$m resulting in a width to pitch ratio of $w/p = 0.8$, the height is 400 nm.

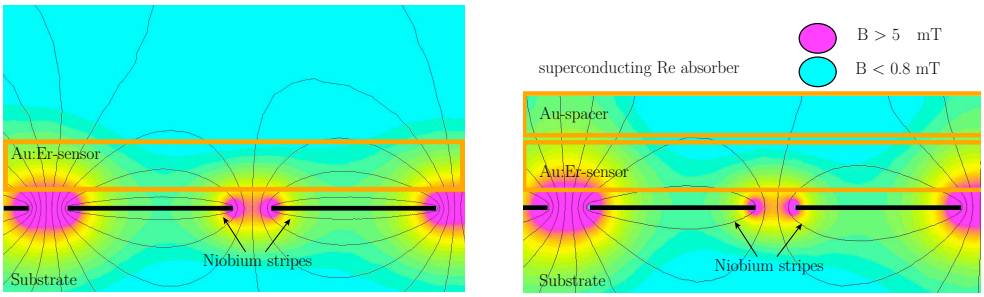

Figure 3.14 Simulated magnetic field distribution. Left: without a superconducting plane above the meander. Right: including a superconducting plane above the sensor.

[3]Acronym for Finite Element Methods Magnetics. Freeware written by David Meeker; http://femm.berlios.de

The same simulation was done for a setup including a superconducting rhenium absorber above the sensor. The meander shaped pickup loop is approximated by eight infinitely long niobium stripes assumed to be superconducting and perfectly diamagnetic ($\chi = -1$). The current is flowing with alternating polarity in successive stripes. Introducing this diamagnetic plane (implemented by setting the vector potential $\boldsymbol{A} = 0$) into the simulation alters the field distribution. Magnetic field cannot penetrate into the absorber, the field is pushed into the sensor increasing the mean field within it for an identical persistent current I_0. This should improve the detector's signal size. Figure 3.14 shows the distribution of magnetic fields found in the sensor for a detector with a 5 μm thick Au:Er foil separated by 1.5 μm glue layer from the SiO_2 covering the meander structure. The same distribution is displayed considering a superconducting plane about 15 μm above the meander. In both simulations an identical persistent current $I_0 = 100\,\mathrm{mA}$ is used. From these results it can easily be seen that the magnetic field at the position of the superconducting plane at is far below the critical field of rhenium.

To find out the important magnetic field distribution the absolute value of the magnetic field B is determined for several thousand points within the sensor. The quantity $P(B)\mathrm{d}B$ gives the probability to find a magnetic field with absolute value B within the interval $[B, B + \mathrm{d}B]$ (the distribution shall be normalized by $\int P(B)\mathrm{d}B = 1$).

3.5.4 Change in Mutual Inductance

Another property of the setup will depend on the magnetic field distribution close to the meander. The used setup consists of the meander shaped pickup loop and a niobium feedback coil a few hundred nanometers above the meander. Their mutual inductance can be measured indirectly as the voltage per flux quantum. The mutual inductance itself depends on the magnetic field distribution generated by either structure within the other one. If a superconducting plane is present in close vicinity to both structures the mutual inductance will change and thus also the voltage drop per flux quantum. With a FEMM simulation it is possible to estimate the relative change in mutual inductance if a superconductor is placed above the structure. Clearly this will strongly depend on the distance of the superconducting plane to the other structures. The result of such a simulation can be seen in Figure 3.15.

3.6 Noise Contributions

In a metallic magnetic calorimeter there exist three intrinsic noise sources. The most fundamental noise source is that of thermodynamic energy fluctuations between subsystems of the detector as described in section 3.2. The second source a magnetic calorimeter will be susceptible upon is magnetic Johnson noise. This contribution to the noise is generated by thermal motions of electrons in adjacent conductors and will be discussed in the following. Finally the employed SQUIDs within the setup also contribute flux noise, the level of which will be discussed in section 4.2.3.

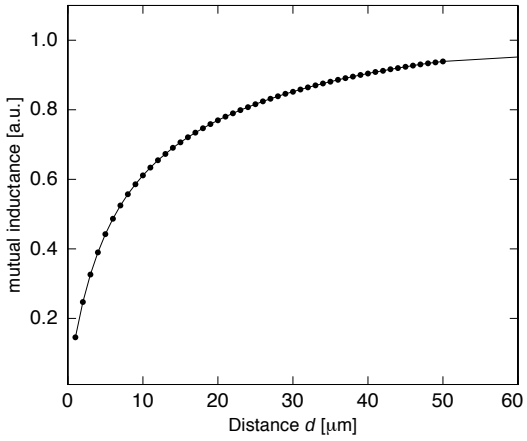

Figure 3.15 Result of a FEMM simulation showing the relative change of mutual inductance between the feedback coil and the pickup loop as a function of distance of a superconducting plane above.

3.6.1 Magnetic Johnson Noise

A permanently existing noise source in metallic magnetic calorimeters is magnetic Johnson noise. It is noise in the magnetic field which is generated by thermal motion of electrons in a conductor. A detector with a metallic sensor or any other conductive material in close vicinity to a pickup loop especially designed to detect flux changes is naturally susceptible to such a noise source. For a more complete understanding of the entire setup with respect to noise the contribution of magnetic Johnson noise can be estimated by simulations. Fluctuating currents in a conductor will generate flux noise in a nearby loop. Calculating this can be done using the fluctuation dissipation theorem [Har68]. An alternating current with frequency ω in a coil generates a magnetic field. Losses associated with eddy currents within the conductor can be described by an apparent resistive impedance $R(\omega)$ of the coil. The resistive part of the loop's impedance can then in turn be used to deduce the flux noise in the coil or loop. According to the Johnson-Nyquist theorem the spectral density of voltage noise of a resistance R at temperature T is $S_U = 4k_\mathrm{B}TR$. The voltage across a superconducting coil and the flux through it are interrelated by $U(\omega) = \omega\Phi(\omega)$. So the root mean square flux noise per root Hertz is given by

$$\sqrt{\mathcal{S}_\Phi} = \frac{1}{\omega}\sqrt{\mathcal{S}_U} = \left(4\pi k_\mathrm{B}T\frac{R(\omega)}{\omega^2}\right)^{1/2}. \tag{3.28}$$

In general the function $R(\omega)/\omega^2$ has a plateau for low frequencies and will drop to zero towards frequencies for which the skin depth has decreased enough to substantially exclude the applied field from the interior of the conductor. The height and cut-off frequency will depend on the distance from the pickup geometry, the volume of the conductor and finally on its conductivity. To obtain the noise of the setup due to magnetic Johnson noise the resistive impedance of any conductor close to the meander shaped pickup loop needs to be known.

The resistive impedance of any conductor in the vicinity of the pickup loop can be obtained by FEMM simulations. The meander geometry is used again but this time an ac current flowing in it. The imaginary part of the impedance $L = L' + iL''$ can

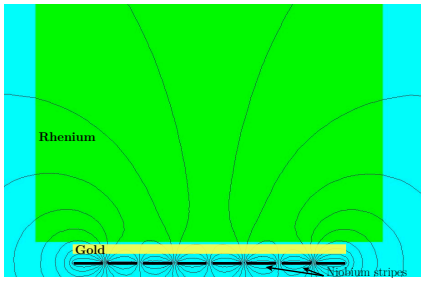

Figure 3.16 The resistive impedance is obtained by numerically calculating the integral $\int \boldsymbol{A}\cdot\boldsymbol{j}\,\mathrm{d}V$ within the conductors close to the meander. Here a rhenium absorber (green) and a gold spacer (yellow) are depicted. For both areas integrals are calculated to estimate their Johnson noise in the pickup loop.

now be obtained numerically. Integrating the scalar product of the vector potential $\boldsymbol{A}$ and current density $\boldsymbol{j}$ in the conductor (seen in Figure 3.16) and dividing this by the amplitude of the ac current I_0 flowing in the meander leads to

$$L''(\omega) = \frac{\int \boldsymbol{A}\cdot\boldsymbol{j}\,\mathrm{d}V}{I_0^2}. \tag{3.29}$$

Combining (4.2.3), (3.29) and the mentioned interrelation between voltage and flux one obtains the measurable spectral flux noise of

$$\sqrt{S_\Phi} = a\sqrt{4k_\mathrm{B}T\frac{L''(\omega)}{\omega}} = a\sqrt{4k_\mathrm{B}T\,\frac{\int \boldsymbol{A}\cdot\boldsymbol{j}\,\mathrm{d}V}{I_0^2\omega}}, \tag{3.30}$$

where a is a constant dependent on the pickup geometry. In the design studied in this work (see Figure 3.13b) the factor becomes to be $a = 1/2$ because two identical meanders are connected in parallel and thus just half the flux noise is measured by the SQUID. The result of such a simulation for the noise contribution of a single crystal rhenium cuboid ($250 \times 250 \times 500\,\mu\mathrm{m}^3$) with a residual resistance ratio of RRR = 800 and of a gold foil ($200 \times 200 \times 5\,\mu\mathrm{m}^3$; RRR = 50) is shown in Figure 3.17.

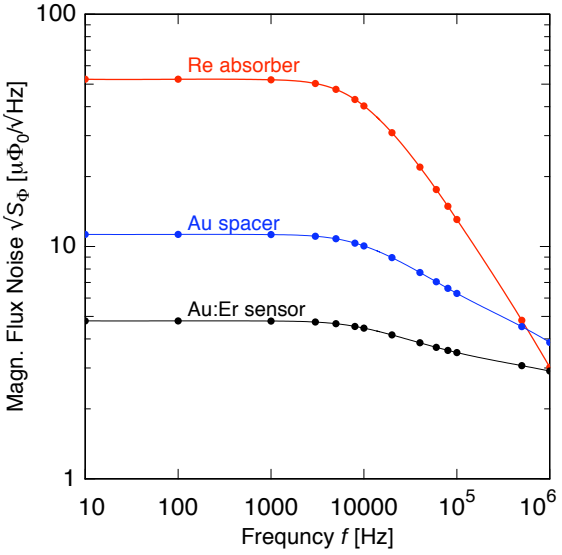

Figure 3.17 Noise contributions of a normal conducting rhenium cuboid ($250\times250\times500\,\mu\mathrm{m}^3$, RRR = 800) and a gold foil ($200\times200\times5\,\mu\mathrm{m}^3$, RRR = 50) gained by a simulation described in detail in the text.

$1/f$ Noise

Another contribution is often observed. For a detector at low frequencies a mainly temperature independent noise contribution that follows a $1/f$ behavior is mostly observed [Fle05]. The noise level of this contribution rises with the concentration x of ions [Dan05] but its origin is not completely explained. One reason might be found in the interaction among spins that can be observed in spin glasses. This correlation would lead to a $1/f$ noise contribution but the transition to a spin glass is expected for much lower temperatures. Another reason could be the interaction of the nuclear quadrupoles of the gold atoms with the magnetic moments of the erbium ions. Further examination of this is needed in form of experiments with a different host material lacking a nuclear quadrupole moment like silver ($I = 1/2$).

4. Experimental Methods

4.1 Cryogenics

The detector system described in the previous chapter requires a working temperature below 100 mK in order to allow for an energy resolution in the range of a few eV. In the context of this work an adiabatic electron spin demagnetization refrigerator (ADR) has been used and will be discussed in this section.

Any process of refrigeration can be thought of as a process of entropy reduction. A system in which the entropy is controllable by an external influence will be useful for the purpose of refrigeration. The magnetic field dependency of the entropy of a system of magnetic moments is the key to magnetic cooling. Paramagnetic salts are suitable refrigerants for magnetic cooling, they contain ions with electronic magnetic moments μ which show little interaction with their surroundings compared to their thermal energy $k_{\mathrm{B}}T$. Each ion in the salt can thus be treated as being independent leading to a molar entropy of the spin system of

$$S = R\ln(2J+1), \tag{4.1}$$

where R is the ideal gas constant and the the total angular momentum J determines the degeneracy $2J+1$ of the ion's energy levels.

With the help of the entropy-temperature diagram in Figure 4.1 it is possible to understand the principle of adiabatic demagnetization. Pre-cooling to liquid ^{4}He temperature or even below by pumping on the helium bath gives a starting temperature between 4.2 K and 1.5 K. This temperature and zero magnetic field are the starting point (A) of the cooling process. From (A) to (B) the salt pills are isothermally magnetized with a superconducting magnet providing a field of up to 6 T. As the magnetic field is applied the degenerate spin states undergo a Zeeman

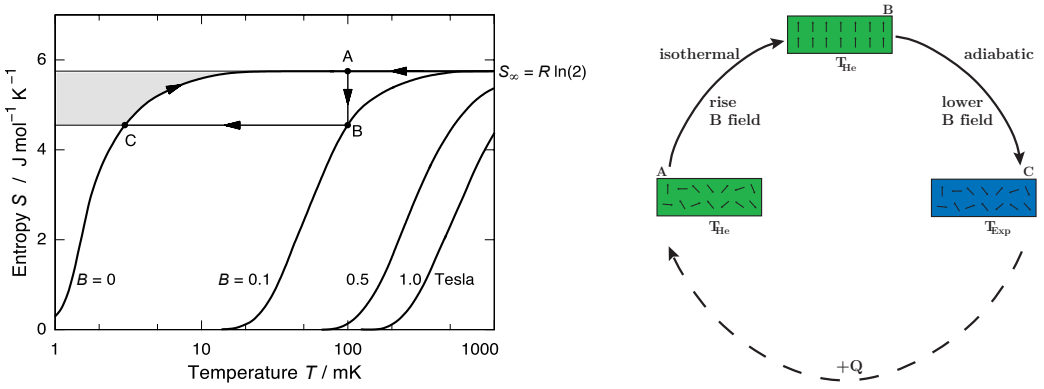

Figure 4.1 Left: Entropy as a function of temperature for the single crystal paramagnetic salt cerium magnesium nitrate (CMN) in different magnetic fields [Ens05]. Right: The three stages in a magnetic cooling cycle.

splitting. When the splitting energy is larger than the thermal energy $g\mu_B B > k_B T$ in equilibrium a large fraction of the spins occupy the energetically lower states leading to an ordering of the spins and thus to a decrease of the entropy S. The heat of magnetization is absorbed by the He-bath. After thermal equilibrium between the heated pills and the bath is reached the paramagnetic salt and the experimental platform attached to it are thermally isolated from the rest of the cryostat.

In the cryostat used for the experiments discussed in this chapter the coolant is suspended from the helium platform by Kevlar strings which are poor thermal conductors (see Figure 4.2). The thermal isolation is achieved by opening a mechanical heat switch. Next the magnetic field is ramped down slowly ($B \rightarrow 0\,\mathrm{T}$), permanently obtaining a thermal equilibrium between the spin and lattice system – the salt pills are adiabatically demagnetized. In the entropy temperature diagram this corresponds to a path along (B) $\rightarrow$ (C). The entropy is held constant and the temperature decreases accordingly.

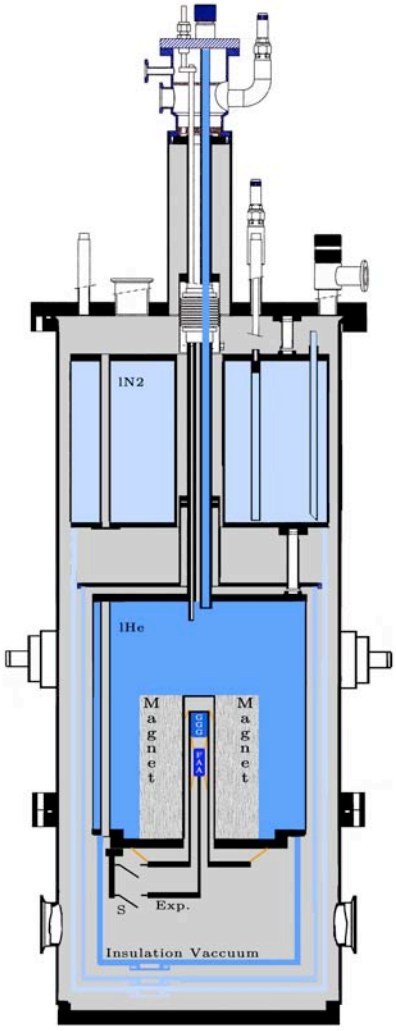

Figure 4.2 Schematic of the ADR used. Insulation vacuum is shown grey, components at liquid nitrogen temperature are depicted in light blue. Those at temperatures of the (pumped) helium bath are dark blue. One more temperature shield is implemented to reduce heat input by radiation (medium blue). One paramagnetic salt pill labeled GGG is suspended from the He temperature platform while a second pill (FAA) is suspended from the GGG temperature platform. This two stage setup reduces the heat load on the cold experimental area providing longer cold phases. Both the GGG and FAA salt pill can be thermally connected with a mechanical heat switch (S) to the thermal reservoir of the helium bath. The pills are surrounded by the superconducting magnet embedded in the helium bath.

Because the described process of refrigeration is not continuous but an entire cooling cycle starting at the helium bath temperature is needed to reach low temperatures again the heat load on the experimental platform needs to be reduced as much as possible. In the cryostat discussed here, a double stage salt pill operating with two salts (GGG[1] and FAA[2]) in a single magnet is installed. Larger internal fields in the GGG pill lead to a higher heat capacity of this pill compared to the FAA. After demagnetization the GGG pill reaches a temperature of around 250 mK. At this temperature it serves well as an intermediate temperature stage. Here all thermally conducting devices that connect the helium bath platform and the experimental platform can be heat sunk. In this configuration the experimental platform connected to the FAA pill can reach a temperature down to 22 mK. The experimental platform connected to the FAA pill will still be exposed to a finite heat load due to internal and external heat loads such as radiation from higher temperatures and dissipation within the experimental setup itself. After complete demagnetization the system will follow the path (C)→(A) in the entropy versus temperature diagram at a minimal warming rate of 0.1 mK/h.

4.2 Superconducting Magnetometer

A technical requisite for the realization of a magnetic calorimeter is a sensitive, low noise and high bandwidth magnetometer. Currently SQUIDs[3] are the most sensitive measuring devices for magnetic flux. In these instruments the interference of the macroscopic wave function of superconductors is exploited. A detailed discussion of SQUIDs can be found in [Cla04] and references within it. In the following a brief introduction on dc-SQUIDs is given and some further properties, needed for the understanding of the experimental setup are discussed. These principles are illustrated by measurements made during this work.

4.2.1 dc-SQUID

A dc-SQUID can be used as a sensitive flux-to-voltage converter and thus is a very sensitive detector of magnetic flux, electrical current or any other physical quantity that can be converted into magnetic flux. A schematic of a SQUID is shown in Figure 4.3. It consists of a superconducting loop with two regions of weak superconductivity – the Josephson junctions or weak links. In parallel to each junction a shunt resistor avoids hysteretic behavior of the device.

The weak links are short enough for Cooper pairs to tunnel through the barrier maintaining their phase coherence. If small currents up to a critical current I_c are driven through the device, the current can be carried by tunneling Cooper pairs and there is no voltage across the junctions. Above this critical current, as the described mechanism cannot carry the applied current anymore, the voltage across

[1] Acronym for **G**adolinium **G**allium **G**arnet: $Gd_3Ga_5O_{12}$
[2] Acronym for **F**erric **A**mmonium **A**lum: $Fe_2(SO_4)_3(NH_4)_2SO_4 \cdot 24H_2O$
[3] SQUID is the abbreviation for **S**uperconducting **QU**antum **I**nterference **D**evice

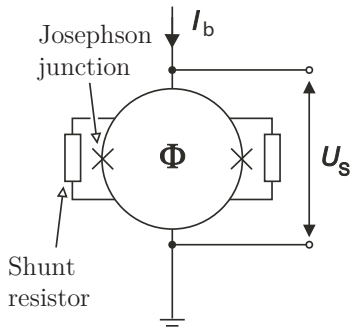

Figure 4.3 Schematic of a SQUID.

the junctions rises sharply. This regime can be described with a dynamic resistance $R_{\mathrm{dyn}} = \partial U/\partial I_{\mathrm{b}}$. For even larger bias currents I_{b} the dc-SQUID asymptotically approaches an ohmic behavior with a slope dictated by the shunt resistors. The critical current depends on temperature, the geometry of the tunneling barriers and on the magnetic flux inside the SQUID loop. Figure 4.4 (left) shows the current-voltage characteristics of a SQUID used in this work.

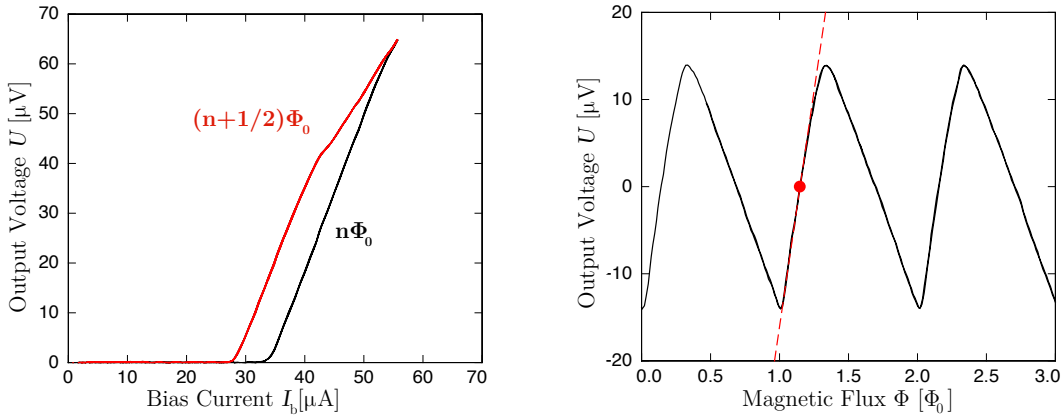

Figure 4.4 Measured I-V characteristics (left) of a detector SQUID and the resulting voltage-flux characteristics (right) for a bias current of $I_{\mathrm{b}} = 37\,\mu$A. The slope at the marked working point is $V_\Phi = (\partial V/\partial\Phi)_I \approx 100\,\mu\mathrm{V}/\Phi_0$.

The I-V curve was measured for two different values of magnetic flux $\Phi = (n + 1/2)\Phi_0$ and $\Phi = n\Phi_0$. Additionally, if I_{c} is exceeded magnetic flux can penetrate into the ring. Due to the Josephson effect, the dc-voltage across the SQUID oscillates (for a fixed bias current I_{b}) as the magnetic flux Φ through the inductance L_{s} of the SQUID loop is increased. The period is given by the magnetic flux quantum $\Phi_0 = h/2e = 2.07 \cdot 10^{-15}\,\mathrm{Vs}$. This behavior is shown in Figure 4.4 (right), for which the voltage-flux characteristic was measured. Generally a SQUID is operated at a steep point of the V-Φ characteristic, where the absolute value of the transfer coefficient $V_\Phi = (\partial V/\partial\Phi)_I$ is a maximum. Therefore, in response to a small input flux $\delta\Phi \ll \Phi_0$ the SQUID produces an output voltage, and effectively is a flux-to-voltage converter.

The linear regime of the SQUID as a flux-voltage transducer is limited to a fraction of about 25% of one flux quantum (see Figure 4.4). Therefore a SQUID is mostly operated in a mode called flux-locked loop (FLL) that is schematically depicted in Figure 4.5. In this mode any deviation between the actual SQUID voltage V and the voltage at the working point V_{wp} is amplified, integrated and fed back into the SQUID via a feedback resistor R_{fb} and an additional feedback coil that is inductively coupled to the SQUID.

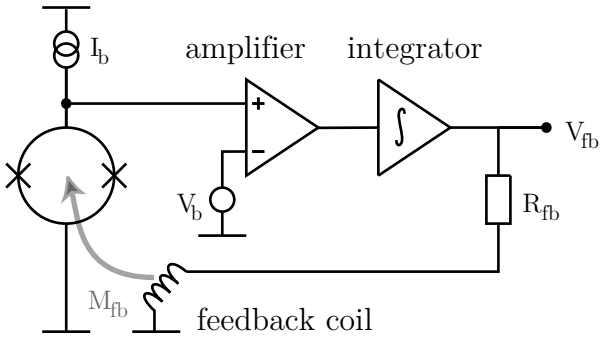

Figure 4.5 Schematic of a flux-locked loop circuit.

This connection scheme compensates any flux change $\delta\Phi$ within the loop by generating an opposing flux $-\delta\Phi_{\mathrm{fb}}$. The voltage $\delta V_{\mathrm{fb}} = \delta\Phi_{\mathrm{fb}} R_{\mathrm{fb}}/M_{\mathrm{fb}}$ across the feedback resistor depends linearly on the applied flux and is used as output signal. In this operation mode the working point of the device can be kept in the linear regime of the characteristic curve and enables one to measure changes over a wide range of fluxes, from a small fraction of a single flux quantum to many flux quanta, only limited by the maximal current in the feedback coil.

4.2.2 Two-stage Configuration

To improve the signal size and reduce the overall noise an alternative readout scheme can be used. A relatively simple method to increase the transfer coefficient of a SQUID is to use another SQUID based low-noise amplifier. Such a configuration is depicted in Figure 4.6.

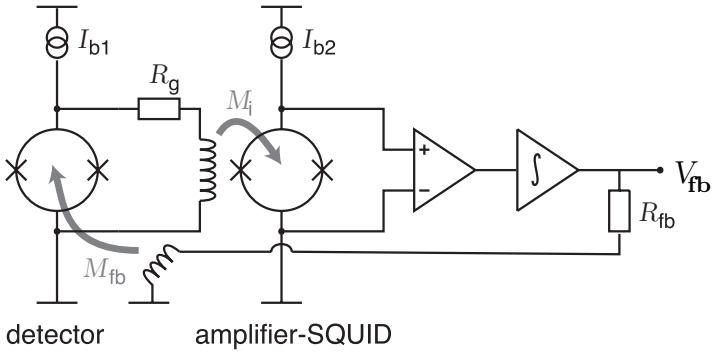

Figure 4.6 Schematic of a two stage SQUID magnetometer with feedback electronics. The primary SQUID is denoted as detector while the secondary is named amplifier.

Both SQUIDs are biased with a current I_{b1} and I_{b2} respectively. A change of flux in the detector SQUID causes a change in current δI_1 flowing through the input coil

of the secondary SQUID. This in turn changes the magnetic flux in the amplifier SQUID by

$$\delta\Phi_2 = M_i \delta I_1, \tag{4.2}$$

where M_i is the mutual inductance of input coil and secondary SQUID. Together with the used gain resistance R_g this leads to a small-signal flux-to-flux amplification of

$$G_\Phi = \frac{\partial\Phi_2}{\partial\Phi_1} = M_i \left(\frac{\partial I_1}{\partial\Phi_1}\right)_{R_\mathrm{g}, I_\mathrm{b}}, \tag{4.3}$$

at the working point. This setup can also be operated in a FLL mode. The voltage drop across the secondary SQUID now is the input of the feedback electronics. The feedback loop is completed by generating a compensation flux in the detector SQUID.

Due to the flux-to-flux gain G_Φ and the transfer coefficient V_Φ of the amplifier SQUID, the contribution of the input noise of the room-temperature electronics to the apparent flux noise of the detector can be greatly reduced.

In most experiments a series-SQUID array[4] was used as a SQUID amplifier. It consists of 16 SQUIDs in series, the voltages are added coherently. This leads to a steep slope at the working point of around $1\,\mathrm{mV}/\Phi_0$.

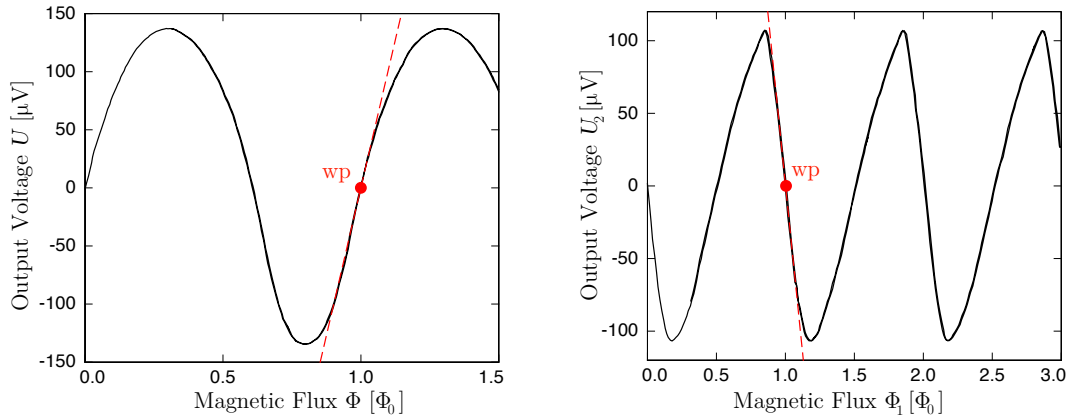

Figure 4.7 Left: Measured SQUID characteristic of the SQUID array used within this work. The slope at the marked working point is $(\partial V/\partial\Phi)_I \approx 1\,\mathrm{mV}/\Phi_0$. Right: Characteristic of the employed 2-stage setup. The shape is slightly asymmetric providing a higher transfer coefficient for a working point on the negative slope, here $(\partial V_2/\partial\Phi_1)_I \approx 930\,\mu\mathrm{V}/\Phi_0$

Figure 4.7 shows the overall two-stage-SQUID characteristics with the mentioned series SQUID array amplifier and a detector SQUID MagCal Nr. 14[5]. The input coupling of the amplifier is only $1/M_i = 23\,\mu\mathrm{A}/\Phi_0$ and the currents provided by the detector SQUID are by far too low to generate an entire flux quantum in the

[4] C3X16A designed by the Physikalisch-Technische Bundesanstalt (PTB) Berlin
[5] Produced at the IPHT Jena

secondary SQUID. Thus a gain resistor as low as $R_g = 0.27\,\Omega$ was chosen. With this the flux changes in the amplifier are still only within the linear regime and the overall shape is very similar to the shape of the primary SQUID alone, slightly asymmetric reflecting the asymmetric arrangement of the inductances of the used MagCal Nr. 14.

There is one more advantage of a two-stage setup, besides the lowered noise. This is the fact, that in a two-stage configuration the amplifying SQUID provides a low impedance readout of the primary SQUID - the input readout being much lower than achievable by means of semiconductor amplifiers at room temperature. Because in the present case the sensor is mounted directly on the SQUID chip, dissipated power on the chip directly leads to an unwanted increase in temperature of the sensor. For a low ohmic readout less power is dissipated on the detector SQUID and therefore the temperature of the detector is as low as possible in a setup with the given design.

4.2.3 Magnetic Flux Noise

After the discussion of magnetic Johnson noise in section 3.6.1 now the contributions of the SQUIDs and the electronics are discussed. A dc-SQUID shows an intrinsic flux noise due to thermal Nyquist noise in the shunt resistors. This noise is mainly independent of frequency but depends on the SQUID's inductance L_s and the working temperature. Numerical calculations for the intrinsic flux noise for an optimized dc-SQUID have been made and the following expression approximately describes this noise contribution (see [Tes77])

$$\sqrt{S_\Phi^{\mathrm{SQUID}}} = \frac{\partial \Phi}{\partial U}\sqrt{S_U^{\mathrm{SQUID}}} \simeq L_s \sqrt{16 k_B \frac{T}{R}}. \tag{4.4}$$

A similarly characteristic parameter to describe the spectral noise density of a SQUID is the so called energy sensitivity that can be expressed as

$$\epsilon_s = \frac{S_\Phi^{\mathrm{SQUID}}}{2L_s}. \tag{4.5}$$

Inserting typical values for the SQUID inductance, $L_S = 200\,\mathrm{pH}$, and the resistance $R = 4\Omega$ at 4.2 K and 50 mK the flux noise would result to $\sqrt{S_\Phi} = 1.47\,\mu\Phi_0/\sqrt{\mathrm{Hz}}$ and $\sqrt{S_\Phi} = 0.16\,\mu\Phi_0/\sqrt{\mathrm{Hz}}$ respectively. Inserting this into (4.5) the energy sensitivity of such a device would be $< 1h$ showing that the approximation of (4.4) will not hold for temperatures that low, due to quantum physical limitations.
The overall apparent flux noise of a two stage setup described so far can be written as

$$S_\Phi = S_{\Phi,1} + \frac{4k_B T R_g}{(\partial U_1/\partial \Phi_1)^2_{R_g}} + \frac{S_{\Phi,2}}{G_\Phi^2} + \frac{S_{U,\mathrm{el}}}{(\partial U_2/\partial \Phi_2)^2 G_\Phi^2}. \tag{4.6}$$

The first and third term represent the intrinsic flux noise of the detector and amplifier SQUID respectively. The second term describes the resistive noise of the gain resistor R_g. The last term gives the contribution of the room temperature electronics, whose input voltage noise $S_{U,\mathrm{el}}$ contributes to the apparent flux noise. In (4.6) it can be seen

that the contribution of the read out electronics is getting smaller with increasing flux-to-flux amplification and for a higher transfer coefficient. This contribution can thus be strongly suppressed by employing a two stage setup as described in the preceding section.

4.3 Detector Design

In chapter 3 the theoretical background of the detector was given. In the preceding sections the basic experimental techniques were discussed and illustrated with a characterization of the employed instruments. The knowledge from these parts shall now be combined leading to a detailed description of the detector setup.

4.3.1 Meander with Integrated dc-SQUID

The detector prototype developed in the framework of this thesis combines the two most important instruments needed for a MMC in one device: it combines the meander with the dc-SQUID in one integrated design – the MagCal Nr. 14, which was previously developed in collaboration with the IPHT Jena for X-ray detectors with larger heat capacity. The layout is shown in Figure 4.8 as microscopic photograph and as a schematic.

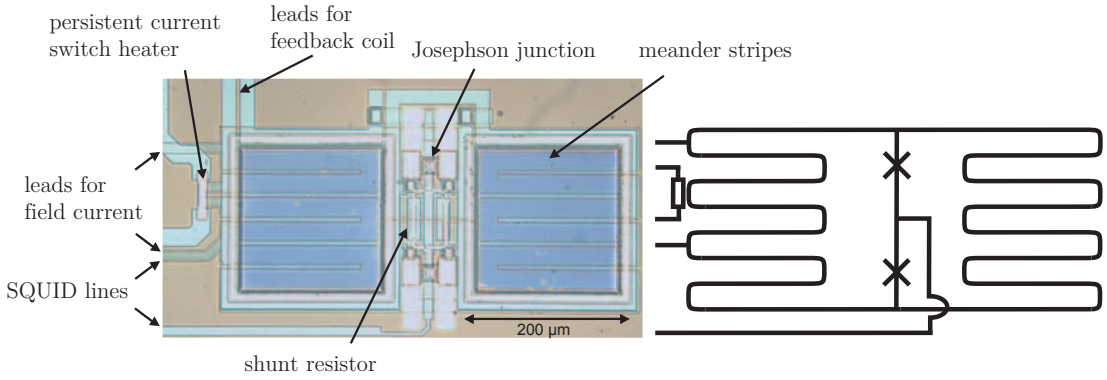

Figure 4.8 Left hand side shows a microscopic photograph of the MagCal Nr. 14 described in the text. On the right a schematic is shown; here the shunt resistors as well as the feedback coil is not sketched.

There is not much of a difference comparing the used layout to the standard dc-SQUID loop discussed in 4.2.1 but the inductance of a MagCal Nr. 14 SQUID consists of two identical meander shaped loops in parallel. Each loop consists of eight stripes of width $w = 20\,\mu$m, the stripes are $5\,\mu$m apart resulting in a pitch of $p = 25\,\mu$m. The total area of one meander extends over an area of $200\,\mu\text{m} \times 200\,\mu\text{m}$. The entire MagCal Nr. 14 chip is $2.5\,\text{mm} \times 2.5\,\text{mm}$ and features four of the described SQUIDs.

In Figure 4.4 the SQUID characteristics showed to be slightly asymmetric, considering the layout this can now be understood. As the leads for the bias current are

not mounted symmetrically their lengths to both Josephson junctions are different. As a matter of fact the bias current will generate flux within the SQUID loop. When changing the flux in the SQUID loop the current in the loop changes periodically and the flux generated by this current can be observed as an asymmetry in the SQUID characteristics.

Obviously one meander shaped inductance in combination with the Josephson junctions would be sufficient to function as a SQUID. However the meander shaped loop is also supposed to function as a generator of magnetic field for the paramagnetic sensor of the MMC. In order to inject a persistent current in the circuit a second inductance in parallel is needed. In the present case this is realized by a second identical meander shaped loop. This gives room for a further development towards a two pixel detector. As a consequence of Kirchhoff's rules it also means that just half of the flux change within one of the loops will be detected by the SQUID as an effective flux change decreasing the total signal size. On the other hand the SQUID inductance is just one half of the inductance of one meander and as discussed in section 4.2.3 this reduces the flux noise $\sqrt{S_\Phi}$ of the SQUID itself by a factor of $\sqrt{2}$.

Figure 4.9 shows the principle of preparing a persistent current. In the following this procedure is explained going from left to right. First a current I_a is injected into

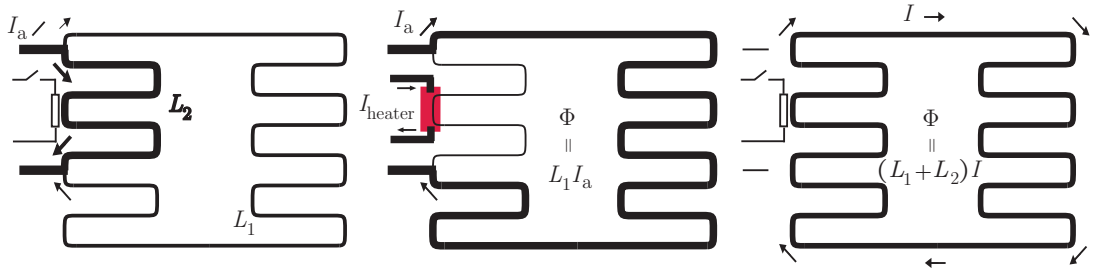

Figure 4.9 Three steps towards preparing a persistent current in the MagCal Nr. 14.

the field current lines. The superconducting loop can be divided into two parts, a shorter one with the inductance L_2 and a second one with inductance L_1. As the loop is superconducting and flux needs to be conserved the applied current splits up according to the inductances L_1 and L_2. Secondly, current is applied to the heater. This current is increased till superconductivity of the niobium structure close to the heater breaks down. Since L_2 will now be normal conducting and thus has a finite resistance, the applied current will flow along the inductance L_1. Furthermore, the superconducting loop is discontinued and magnetic flux $\Phi = LI_a$ can penetrate into it. Thirdly, the heater is switched off and the superconducting loop is continuous again. The flux trapped within it needs to be conserved. After turning the field current off a current I needs to flow through the meanders' total inductance $L_1 + L_2$

$$L_1 I_\mathrm{a} = \Phi = (L_1 + L_2)I. \tag{4.7}$$

Because of flux conservation and according to the inductances L_1 and L_2 this current

can be written as

$$I = \frac{L_1}{L_1 + L_2} I_\mathrm{a}. \tag{4.8}$$

Just by approximating the magnitude of the two inductances L_1 and L_2 by their geometrical length the ratio in 4.8 will be of the order of 3/4. The persistent current I actually generated by the flux trapped inside the meander is about 25% less than the applied current I_a. One needs to recall this when comparing simulated and measured data.

4.3.2 Detector Setup

In the following the setup of the detectors employed during this work will be described. Figure 4.10 shows a 3-dimensional drawing of one of the detectors built.

All important components of the detector are attached to a brass holder designed for this experiment. It features an underneath grove and a hole through which pass some of the electrical connections for the detector chip. The holder is arranged to be inside a lead shield. Lead becomes superconducting at 7.2 K; since within a superconducting loop the magnetic flux is conserved, the lead is supposed to shield the experiment against external variations in magnetic field. A lead shield is also used for the amplifier SQUID array, in this case a supplementary shielding made of soft magnetic Metglas foil[6] was placed around the lead shield. That way it is possible to not only keep the magnetic field inside constant but also to assure a very small absolute value of the magnetic field. The brass holder together with the lead shield is screwed to the experimental platform attached to the FAA pill of the cryostat.

The brass holder also hosts a purposefully designed circuit board. On this board the leads for the feedback lines and the SQUID are realized with copper circuit paths. On the one side those can be connected via a plug to the secondary SQUID, on the other side it leads directly to the detector chip. The other input leads for the field lines of the meander and for the persistent current switch heater were achieved in a different way. The currents needed for those parts of the detector are comparably large. To reduce parasitic heating the connections ought to be superconducting. Four NbTi/CuNi[7] wires of typically 50 μm to 100 μm diameter were routed through the hole in the brass holder and anchored there with adhesive[8]. Those wires were filed down to create a bond pad for the connection to the chip.

The MagCal Nr. 14 chip is mounted onto the holder with low-temperature suitable varnish[9]. All connections between the field and heater lines, the circuit board and the detector SQUID chip are ultrasonically wedge bonded with aluminum wire of diameter 25 μm.

Different types of sensor/absorber configurations were built during this work. In

[6] Alloy 26055A1 manufactured by Metglas Inc., Conway
[7] The superconducting niobium-titanium filaments are implemented into a copper-nickel matrix.
[8] A two component epoxy was used: STYCAST 2850 FT, by Emerson & Cuming
[9] GE Varnish 7031

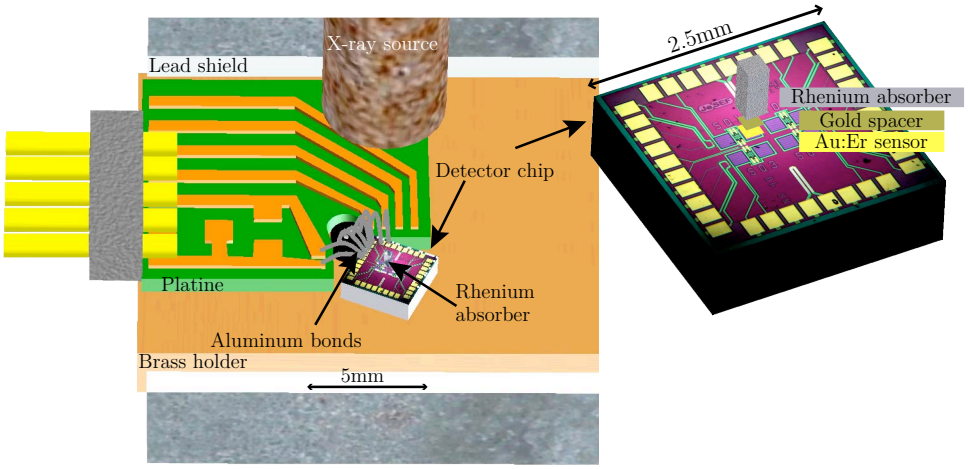

Figure 4.10 The figure shows a 3-dimensional drawing of the detector setup described in the text. On the right hand side a detailed view of the MagCal Nr. 14 SQUID chip can be seen as well as an explosive view of the detector layers comprising of the Au:Er sensor, the gold spacer and the rhenium absorber are indicated as such.

one type a Au:Er-sensor foil covering an area of $200\,\mu\text{m} \times 200\,\mu\text{m}$ and $5\,\mu\text{m}$ thickness was glued with a thermally conductive adhesive[10] onto the meander opposite the heater. The foil was mechanically pressed onto the meander to ensure a lowest possible distance to the meander. The Au:Er sensor featured a concentration of isotopically enriched erbium of 600 pp.. Although the magnetic field decreases exponentially with the distance from the meander a spacer was introduced to make sure the rhenium absorber will only be exposed to fields by far smaller than the critical field of rhenium. As a spacer a gold foil of the same area and $5\,\mu\text{m}$ thick is glued and pressed onto the sensor foil. This spacer contributes to the overall heat capacity of the detector. With an electronic heat capacity of $1.1\,\text{pJK}^{-1}$ (at 50 mK) this may not be neglected. On top of the spacer a single crystal rhenium cuboid ($\approx .250 \times 250 \times 400\,\mu\text{m}^3$) was glued.

In another setup the design in principle is the same. As before the rhenium cuboid is separated from the Au:Er sensor by a $4\,\mu\text{m}$ thick gold layer. Unlike in the previously described setup the layers were not glued onto each other. Here they were directly sputter deposited onto the rhenium absorber. In this process, surface atoms of the so called sputter target are ejected by bombardment with energetic argon ions from a plasma. The ejected atoms recondense from the gas phase as a thin film on the substrate in the sputtering chamber. A single crystal rhenium[11] was cut in cuboids of about $250 \times 250 \times 500\,\mu\text{m}^3$ with a wafer saw and thoroughly lapped with alumina abrasives of different grain sizes. An approximately 120 nm thick layer of copper is first deposited onto the rhenium. This serves as a sticking layer for the following

[10] A two component epoxy was used. STYCAST 1266 A/B , by Emerson & Cuming
[11] Diameter of 8 mm, length 1 mm and 99.999% purity; produced by Goodfellow GmbH.

gold spacer of 4 μm thickness. Finally also the 3 μm thick Au:Er sensor is sputtered onto the spacer. In the end the absorber with integrated sensor is glued onto the SQUID chip using STYCAST 1266. For this detector the sensor has an erbium concentration of 750 ppm with the natural isotopic mixture of erbium. In this setup a nearly completely microfabricated detector was realized. This is a big improvement compared to the other setup described. More precision is gained because less glue layers are needed that are not well defined. With this, reproducibility should be increased and more than single prototype production should be possible. Additional efforts are made to sputter directly on top of the meander. This would give more certainty for the actual thickness of the adhesive droplet between the glued layers and thus about the distance of the sensor to the field generating meander. For the understanding of the data this is an important parameter.

The characterization of the detector properties is more easily achieved by measuring an energy spectrum with discrete lines. To obtain this the rhenium was exposed to the X-rays emitted by a ^{55}Fe source during most of the discussed experiments. The instable isotope ^{55}Fe undergoes an electron capture process and decays to ^{55}Mn, subsequently emitting X-rays with characteristic energies. The two most intense line in this X-ray spectrum are the K_α-line at an energy of 5.9 keV and the K_β-line at an energy of 6.5 keV. For the X-ray irradiation a hole is prepared in the lead shield. In order to reduce the number of X-ray quanta that miss the absorber and hit the substrate, an additional collimator made of circuit board material and a gold foil of 8 μm thickness is prepared with a small hole and placed above the absorber.

4.3.3 Arrangement of the Wiring

The arrangement of the wiring of the two-stage-SQUID setup that was used in this work can be seen in Figure 4.11. Additionally, the different temperature stages of the cryostat (room temperature, liquid helium temperature and temperature of the experimental platform) are shown. As the wires coming from room temperature are made of thermally well conducting copper they need to be heat sunk several times. Components gathered in a light grey area can be found within a superconducting lead shield. The dark grey areas represent the SQUID chips, namely the secondary amplifier chip at helium temperature and the detector itself at lowest temperature. All wires between helium bath temperature and the experimental platform are made of NbTi/CuNi and are heat sunk one more time at the intermediate temperature of the GGG pill to further reduce parasitic heating. The wires are prepared as twisted pairs and twisted triples in order to suppress possible interference from external sources and crosstalk from neighboring wires.

4.3.4 Thermometry and Data Acquisition

The temperature was monitored with resistance thermometers installed on each relevant area of the cryostat. The thermometer installed on the experimental platform is a resistance made of RuO_2 with a $\mathrm{d}\log(R)/\mathrm{d}\log(T)$ value of about -1.5 at 30 mK.

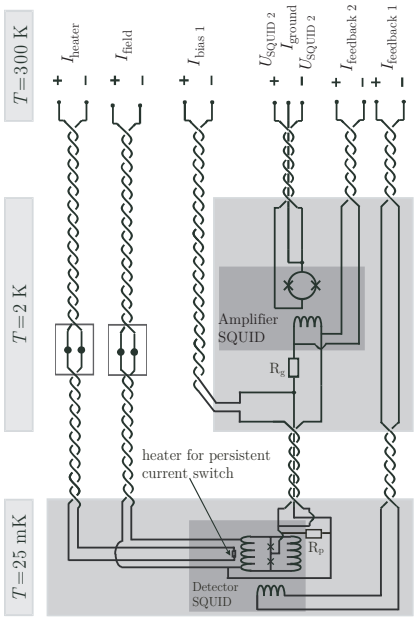

Figure 4.11 Wiring of a detector with a two-stage-SQUID configuration.

An AVS-47[12] resistance bridge was used to measure the resistances, allowing for a temperature determination with an uncertainty of 1.8 μK.

Figure 4.12 shows the data acquisition of detector events schematically. The output of the SQUID is amplified and linearized by the SQUID electronics. Afterwards the signal is split into two channels. One of those is the later recorded signal, the other is used as a trigger channel. Both channels are preprocessed in a low noise amplifier that additionally features a variable second order band-pass filter[13]. The trigger channel can be filtered strongly while filtering of the actual signal implies a modification of the signal shape. For pulse shape analyses this is unwanted, therefore merely a 30 kHz low pass was used in this case.

Through high frequency filters the signals are lead out of the Faraday cage the cryostat is located in. Outside the cage the signals are analog to digital converted by a dual channel oscilloscope card[14]. The trigger level is set for the more strongly filtered channel and when the signal of this trigger channel exceeds the trigger level the acquisition of a pulse from the signal channel is initiated. Each acquired timeframe consists of typically 16384 voltage samples with 12 bit resolution. Usually one quarter of the samples are prior to the trigger.

For a thorough analysis of the noise also baselines are acquired, these recorded timeframes are not triggered by overstepping the trigger level and thus do not contain a pulse shaped signal.

[12]Manufactured by Pico-Watt Electronica, Finland.
[13]Type SRS-560, manufactured by Stanford Research, USA.
[14]Manufactured by GaGe

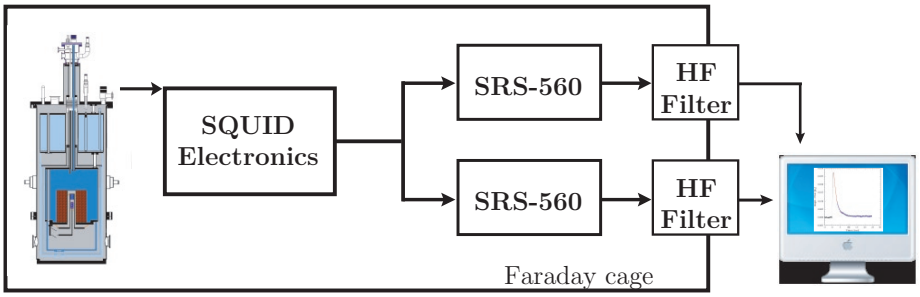

Figure 4.12 Schematic of the data acquisition and the devices used for it.

5. Experimental Results

The results presented in the following were acquired with the detectors described in the previous chapter. The transition temperatures of differently treated rhenium single crystals to the superconducting phase are presented. The intention of this analysis is the understanding of the influence of different processing parameters on the critical temperature of rhenium and consequently achieving reproducibility of rhenium samples with the same critical temperature. Furthermore, detector signals following the absorption of X-rays in the superconducting rhenium are presented. The pulse shape is measured for different experimental conditions and analyzed within the framework of a thermodynamic model that comprises thermal as well as athermal processes.

5.1 Magnetic Flux Noise

5.1.1 Detector Noise at 4.2 K

The noise of a detector consisting of a 2-stage-SQUID readout with a Au:Er sensor, a gold spacer and a rhenium absorber was measured at a temperature of 4.2 K (Figure 5.1).

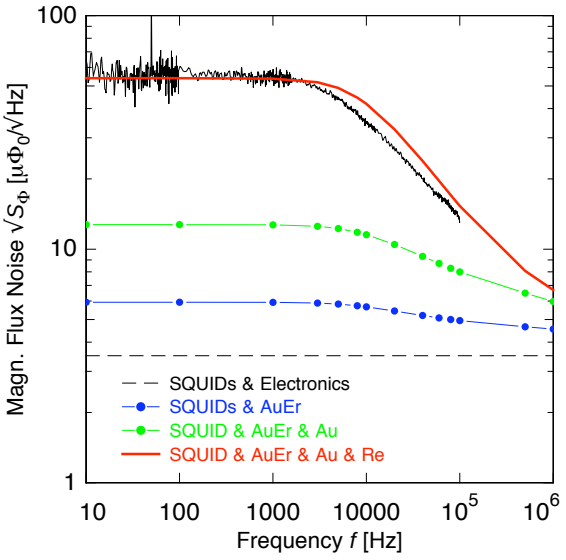

Figure 5.1 Noise of a detector with Au:Er sensor, gold spacer and rhenium absorber measured in a 2-stage configuration at $T = 4.2\,\mathrm{K}$. Additionally, some expected individual noise contributions are shown, as well as the theoretically expected overall noise.

The noise level of the magnetic flux noise at frequencies below 1 kHz is found to be $56\,\mu\Phi_0/\sqrt{\mathrm{Hz}}$. The different noise contributions of the electronics, the SQUIDs and the magnetic Johnson noise caused by the conducting materials are the basis for the understanding of this measurement. The contributions to the apparent flux noise in the SQUID of the employed devices can be estimated using (4.6). The room temperature electronics has a voltage noise of $0.33\,\mathrm{nV}/\sqrt{\mathrm{Hz}}$[1], a gain resistor of

[1] This is the white noise level above 100 Hz. Below this frequency the input voltage noise is

$R_g = 0.27\,\Omega$ was installed. The electronics will show an apparent flux noise in the detector SQUID of $0.37\,\mu\Phi_0/\sqrt{\text{Hz}}$. Considering the very small transfer coefficient ($5.8\,\mu\text{V}/\Phi_0$) of the detector SQUIDs in the low-impedance two-stage configuration, the gain resistor generates a flux noise of $1.37\,\mu\Phi_0/\sqrt{\text{Hz}}$ at $T = 4.2\,\text{K}$ and will scale proportionally to the square root of the temperature. The intrinsic noise of the SQUID array amplifier is $0.4\,\mu\Phi_0/\sqrt{\text{Hz}}$, considering the flux-to-flux gain of 0.87 the contribution to the apparent flux noise in the detector is $\sqrt{S_\Phi} = 0.46\,\mu\Phi_0/\sqrt{\text{Hz}}$. The detector SQUID itself dominates all the noise of the devices with an intrinsic flux noise of $3.2\,\mu\Phi_0/\sqrt{\text{Hz}}$ at this temperature. Adding all these independent noise contributions quadratically leads to a noise level of $\sqrt{S_\Phi} = 3.5\,\mu\Phi_0/\sqrt{\text{Hz}}$.

However the main contribution to the flux noise at 4.2 K is the magnetic Johnson noise of the Au:Er sensor, the gold spacer and the normal conducting rhenium absorber. The contributions of the metallic layers are calculated as discussed in section 3.17. A gold spacer of dimension $200 \times 200 \times 5\,\mu\text{m}^3$ with a RRR=50 contributes $\sqrt{S_\Phi} = 11\,\mu\Phi_0/\sqrt{\text{Hz}}$ and a Au:Er sensor of the same size and a conductivity at 4 K of $\sigma = 2.5 \times 10^8\,\Omega^{-1}\text{m}^{-1}$ contributes a noise of $\sqrt{S_\Phi} = 4\,\mu\Phi_0/\sqrt{\text{Hz}}$. The Johnson noise of a rhenium cuboid ($250 \times 250 \times 400\,\mu\text{m}^3$) with an estimated RRR of 800 is calculated to be $\sqrt{S_\Phi} = 53\,\mu\Phi_0/\sqrt{\text{Hz}}$. Adding all of the above noise contributions quadratically results in a white noise level of $55\,\mu\Phi_0/\sqrt{\text{Hz}}$. Beyond this good understanding of the amplitude of the noise, also the cut-off frequency of the noise shows the expected behavior. The contribution of the rhenium crystal is dominating and from the calculations for frequencies above 5 kHz a cut-off due to the decreasing skin depth is expected. This value is only about 10% higher than observed in the measured spectrum. This can be seen in Figure 5.1 where the theoretically expected noise spectrum (red line) is shown additionally to the recorded noise spectrum (black).

By understanding the individual noise sources the detector can be well characterized and, as will be seen in the next section, the magnetic Johnson noise can be used to study the conductivity of the rhenium absorber.

Furthermore, Figure 5.1 clearly shows that a simple noise measurement at 4.2 K can be used to assure that the rhenium absorber is present above the meander even after the detector was installed in the cryostat and cooled down, a very helpful tool once considering large arrays of detectors.

5.1.2 Detector Noise at Low Temperatures

At the working temperature of the detector many noise contributions are reduced due to their temperature dependence. The noise of the same detector as discussed above, measured at a temperature of the experimental platform of $T = 35\,\text{mK}$, is shown in Figure 5.2. A persistent field current has been been injected in this measurement. The plateau value of the noise at frequencies above 5 kHz is reduced to $\sqrt{S_\Phi} = 2.9\,\mu\Phi_0/\sqrt{\text{Hz}}$. At temperatures below 120 mK low frequency noise contribution becomes visible. The reason for this can be found in temperature variations of the sensor due to the absorption of X-rays [Hau06]. The contributions of the room

$0.46\,\text{nV}/\sqrt{\text{Hz}}$.

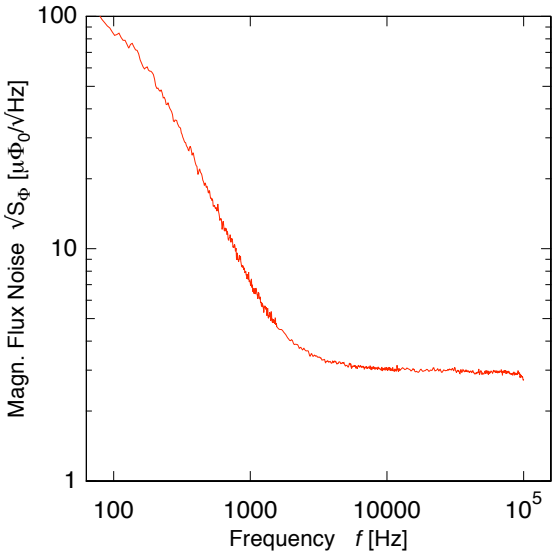

Figure 5.2 Noise of a detector with Au:Er sensor, gold spacer and rhenium absorber measured in a 2-stage configuration at $T = 35\,\mathrm{mK}$.

temperature electronics as well as of the SQUID amplifier remain the same, because they are operated under the same conditions as before. For further understanding one should recall the integrated design of the meander and the SQUID used for the discussed detectors. With this, one will expect a slightly higher local temperature of the entire detector compared to the one indicated by the cryostat's thermometry. A chip-temperature of 50 mK to 60 mK can be assumed for a temperature reading of 35 mK. As we will see later in the magnetization measurements this assumption is reasonable. The largest contribution to the detector noise at these temperatures can be explained by the magnetic Johnson noise of the gold spacer which is around $1.3\,\mu\Phi_0/\sqrt{\mathrm{Hz}}$ for a temperature of 55 mK. The noise contribution of the sensor is negligible. The rhenium absorber at these temperatures is far below its T_c and thus should not contribute to the flux noise at the studied frequencies. The intrinsic noise of the detector SQUID can be estimated as well. Equation 4.4 suggests a decrease in the noise proportional to the square root of the temperature. For $\sqrt{55\,\mathrm{mK}/4.2\,\mathrm{K}}$ on would expect a reduction of this noise contribution by about a factor of 10. This noise is mainly due to the shunt resistors of the SQUID. Because of the continuous biasing of the device and the thermal decoupling of the electrons within the resistors a local temperature of 200 mK to 300 mK can be expected, only leading to a reduction of the SQUID noise by 75% leaving a contribution of $0.8\,\mu\Phi_0/\sqrt{\mathrm{Hz}}$. However, the SQUID noise measured is about $\sqrt{S_\Phi} = 2.5\,\mu\Phi_0/\sqrt{\mathrm{Hz}}$. This is not an uncommon observation for SQUIDs working at very low temperatures. Nevertheless, there is no generally accepted explanation for this behavior. Most likely it is due to intrinsic resonances at the Josephson frequency and harmonics of it. At this stage this needs to be accepted since the used devices are not purposefully designed for temperatures far below 4.2 K.

5.2 Superconducting Transition of Rhenium

Following the previous discussion of noise the temperature dependence of the magnetic Johnson noise of rhenium also contains information about its transition to superconductivity. As the sample changes its conductive properties also the Johnson noise should reflect this in changing its plateau value at low frequencies and the cut-off frequency. As discussed in section 3.6.1 the level of the low frequency plateau will increase as the conductivity rises, at the same time the cut-off frequency is expected to decrease. For the superconductive phase the cut-off frequency will be so low that the noise contribution of the object cannot be observed in the noise spectrum any longer and the white noise level drops to a value according to the sum of the other noise contributions.

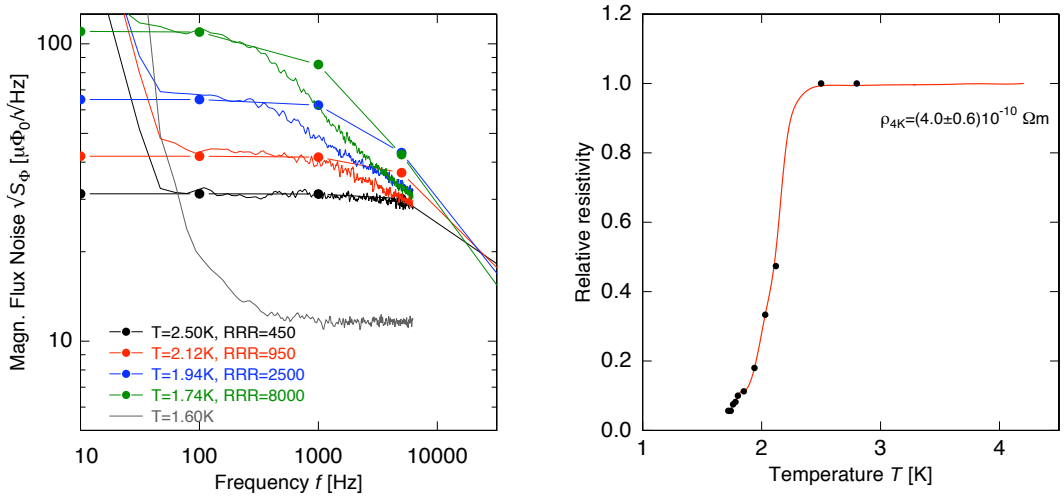

Figure 5.3 Left: Noise measurements of heat treated rhenium crystals in the temperature range of the transition to superconductivity. Also results of FEMM simulations with the denoted residual resistivity ratios are shown for the given temperatures. Right: The extracted relative resistance is shown for the temperature range of investigation. The line connecting the data points serves as a guide for the eye.

The change in noise during the transition can be seen in Figure 5.3. Indeed one can observe the expected qualitative changes of the spectral shape. However, the spectral shape is not described perfectly by the simulated data. A much better agreement on the other hand would be surprising considering the simplicity of the approach. Here a homogenous sample is assumed, uniformly changing its overall conductivity. In this analysis the plateau value at low frequencies was fitted in order to extract a RRR value. Fitting the data with the simulations shows an increase of the residual resistivity ratio by nearly a factor of 20, which corresponds to a decrease in resistivity to about 5% of the starting value.

With the detector constructed initially this behavior could be seen but the transition appeared at a temperature of 2.7 K, about 1 K higher than the literature value. However, such a behavior has been seen before for mechanically stressed rhenium

[Chu68, Hul57]. A heat treatment of the rhenium crystals was shown to give consistent values for the transition temperature of $T_c = 1.7\,\mathrm{K}$.

During this work the physics of the superconducting rhenium absorber and its properties was studied. In order to obtain reproducible results a rhenium sample previously showing a T_c of 2.7 K was annealed for about one hour at a temperature of 1900 K and the annealing procedure showed the wanted effect, i.e. a T_c of 1.7 K.

During the transition to superconductivity not only the shape and amplitudes of the noise spectra change. There are other quantities that change in a characteristic way while cooling the setup through the transition to superconductivity of rhenium. As discussed in section 3.5.4 the voltage per flux quantum in FLL mode measured for the used setup is inversely proportional to the mutual inductance of the feedback coil and the meander shaped pickup loop. If the rhenium absorber becomes superconducting this mutual inductance should decrease, consequently an increase of the voltage per flux quantum is expected. The change in the voltage per flux quantum was measured cooling the setup through the superconducting transition. The results for a heat treated and an untreated rhenium sample are shown in Figure 5.4.

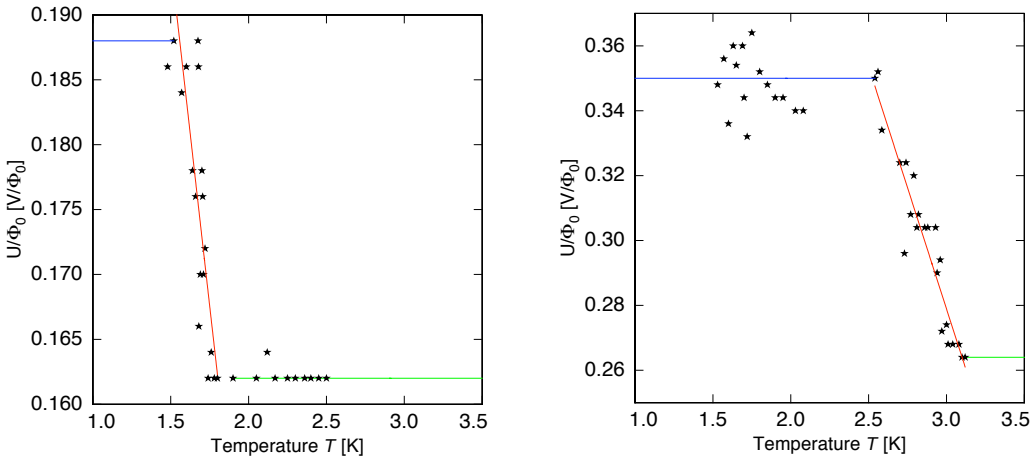

Figure 5.4 The plots show the relative change of the voltage per flux quantum in FLL mode for an annealed rhenium sample (left) and an untreated sample (right).

These measurements clearly show that the described heat treatment effects the transition temperature of rhenium. The heat treated sample shows a transition at $T_c = 1.7\,\mathrm{K}$ whereas the untreated rhenium crystal has a higher T_c of 2.7 K.

It is interesting to notice that by comparing Figures 5.3 and 5.4 the resistivity ρ already dropped to about 5% of its initial value before an effect in the measurement of the voltage per flux quantum can be observed. The latter is only possible when an entire plane close to the meander becomes superconducting. With both measuring methods a decrease in the transition temperature due to the heat treatment is clearly observed.

Though being a detail this result can be of further importance for the understanding of rhenium as a superconducting absorber of an MMC as the energy gap, which is directly related to T_c, is expected to be a parameter of major importance,

e.g. for the quasiparticle recombination times. Consequently, this issue needs to be addressed for the understanding of the thermalization in a superconductor as well as for the reproducible preparation of rhenium absorbers. Furthermore, the data can qualitatively be described by the discussion provided before. A quantitative description of the increase in mutual inductance below T_c is beyond the scope of this work. Still the results of the simulations given in section 3.5.4 could be improved by performing a true 3 dimensional finite element simulation of the detector setup.

5.3 Magnetization Measurements

All the measurements presented in this and the following sections were acquired with the same setup. The detector consisted of a MagCal Nr. 14 chip with a 5 μm thick Au:Er sensor foil glued onto it. On top of this a 5 μm thick spacer and a rhenium absorber were glued.

The temperature dependence of the magnetization of the sensor was measured. Since the magnetization cannot be measured directly the flux change within the SQUID generated by the change in magnetization was measured for temperatures ranging from 35 mK to 400 mK.

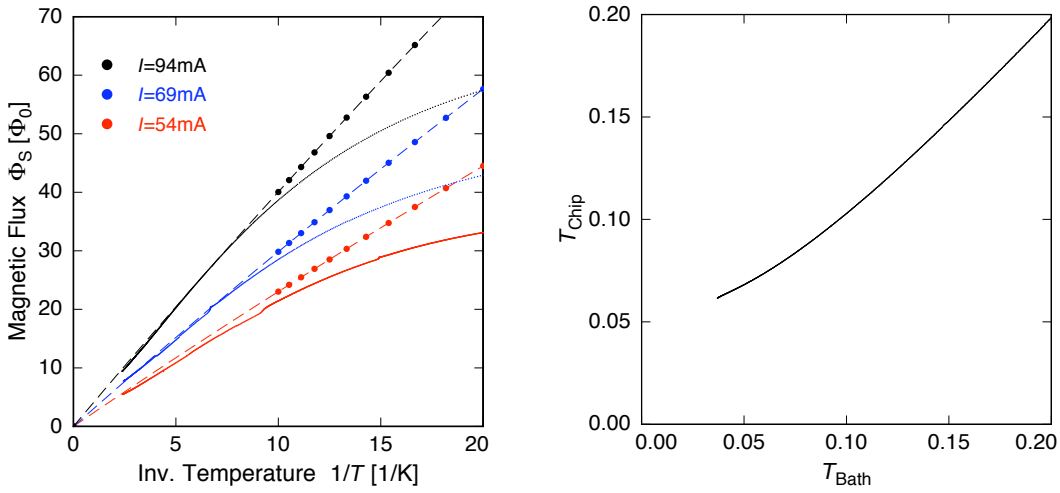

Figure 5.5 Left: Magnetization versus inverse temperature. The dashed lines correspond to results of numerical simulations. Right: Chip temperature as a function of the temperature of the cryostat extracted from the magnetization data for $I = 94$ mA

The change in flux as a function of inverse temperature is shown for three different field generating currents $I_a = 54\,\text{mA}, 69\,\text{mA}$ and $94\,\text{mA}$[2] in Figure 5.5. The theoretically expected change in magnetic flux can be calculated from the field distribution within the sensor and the erbium concentration as described in section 3.5.3. Results of such a simulation are depicted as dashed lines. For these simulations a 1.5 μm

[2] $I = 0.75 I_a$ is used in all analyses.

thick glue layer between the SiO_2 and the sensor was assumed as well as a superconducting plane at the surface of the rhenium absorber that faces the meander. The persistent current was assumed to be 75% of the current applied to the meander when freezing the field current into the structure.
For temperatures above 100 mK the data shows a good agreement with the results obtained from the simulations. Below this temperature the measured data deviates from the calculations. This can be explained by an increased sensor temperature compared to the experimental platform, due to the power dissipation on the SQUID chip. From comparing the measured to the calculated data, a sensor temperature can be extracted and is shown in Figure 5.5 (right). This will be important for all further analyses as the pulse height for a given deposited energy strongly depends on the temperature of the sensor.

5.4 Detection of X-rays With a Superconducting Rhenium Absorber

As mentioned before a ^{55}Fe X-ray source was mounted above the detector. The detector signals caused by the absorption of those X-rays in the rhenium absorber were recorded and will be discussed in the following.

5.4.1 Spectrum

Signals from the detector are recorded as voltage signals with a characteristic evolution in time. In the following these signals will be referred to as pulses. An averaged reference pulse $r(t)$ is created and all other events are compared to this. In order to assign an amplitude A (that will be proportional to the energy absorbed) to every single pulse $s(t)$ the reference pulse $r(t)$ is stretched by the factor A and shifted by an offset A_0 so that the sum of quadratic deviations $\chi^2 = \sum_i (s(t_i) - Ar(t_i) + A_0)^2$ is minimized.

Figure 5.6 shows a scatter plot, where the χ^2-value of each pulse is plotted against its assigned amplitude A. The reference pulse chosen in the underlying analysis was

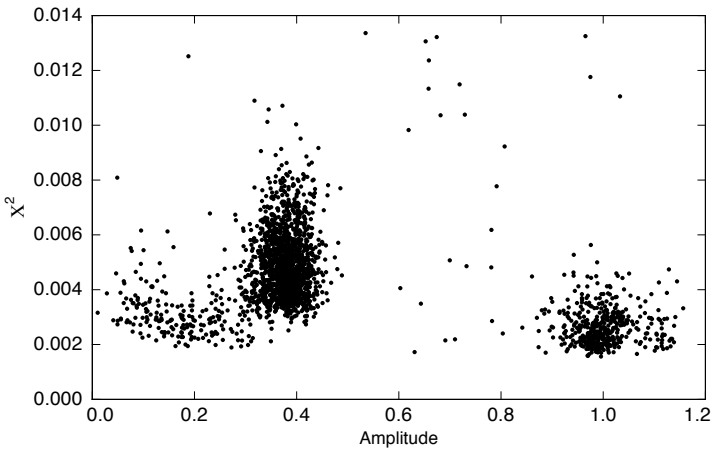

Figure 5.6 Scatter plot of the χ^2-values versus amplitude A for each pulse. The data was taken at a temperature of 34 mK and with a persistent current in the meander of $I = 0.75 \times 125\,\text{mA} = 94\,\text{mA}$. The reference pulse corresponds to a 5.9 keV photon.

generated by averaging pulses that correspond to photons of the K_α-line of ^{55}Mn emitted by the calibration source, which carries an energy of $E = 5.9\,\text{keV}$. There are mainly three areas of high density within this plot: the events close to the amplitude 1.0 and close to 1.1 which belong to the K_α and K_β lines, respectively. Events with an amplitude ranging from 0 to 0.25 correspond to electrons emitted in a β-decay of ^{187}Re. Furthermore, many events can be seen with amplitudes ranging from 0.25 to 0.4. They show a slightly higher χ^2-value resulting from a qualitatively different signal shape. Most likely these signals are caused by photons missing the absorber and hitting the substrate of the detector chip, due to imperfect collimation. By looking at individual pulses, all events with a χ^2 value greater than 0.006 in this data set can be identified to be pile up events. These pulses are excluded from the further analysis. In the following the discussion will concentrate on X-rays absorbed in the rhenium, which means the events that can be found around an amplitude $A = 1$.

5.4.2 Signal Shape

Figure 5.7 shows a typical time pattern of the measured magnetic flux in the SQUID following the absorption of a 5.9 keV X-ray in the superconducting rhenium.

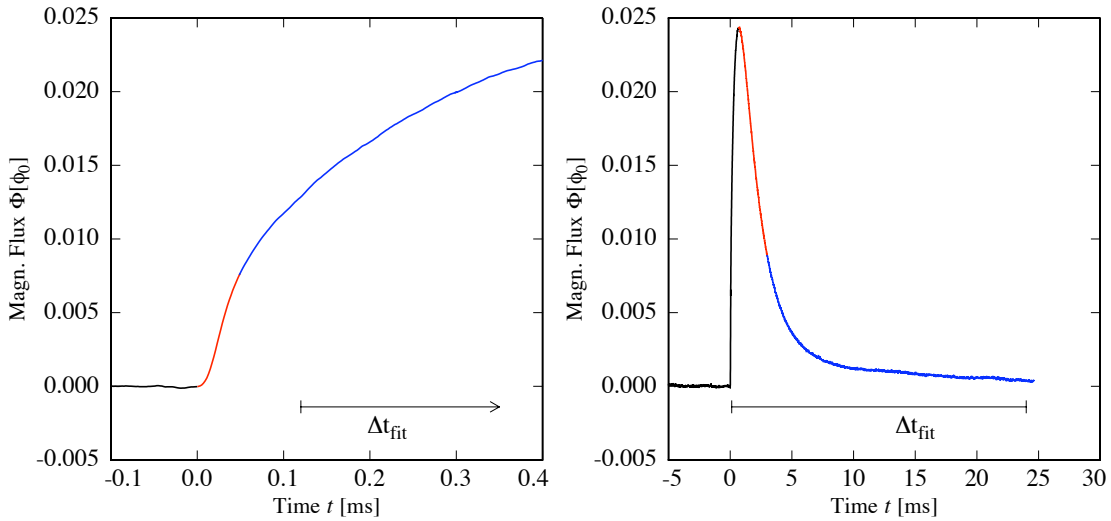

Figure 5.7 Time pattern of the flux signal after the absorption of 5.9 keV X-ray. The generating field current was $I = 94\,\text{mA}$ and the signal was recorded at a bath temperature of $T = 34\,\text{mK}$. On the left hand side a zoom of the first $400\,\mu\text{s}$ of the pulse, shown on the right is depicted. Δt_{fit} corresponds to the time interval used for fitting the pulse.

Both, the signal rise as well as the decay of the signal, can be described by two exponentials, therefore the signal shape can be described by a function of the form

$$s(t) = -a_{\text{f}} e^{-t/\tau_{\text{f}}} - a_0 e^{-t/\tau_0} + a_1 e^{-t/\tau_1} + a_2 e^{-t/\tau_2}, \tag{5.1}$$

where terms containing a_f, τ_f and a_0, τ_0 describe the rise of the signal whereas terms containing a_1, τ_1 and a_2, τ_2 describe the decay. In order to fulfill $s(t = 0) = 0$, the parameter a_f needs to equal $a_1 + a_2 - a_0$.

The signal shape observed with a MMC with a superconducting absorber differs in a very characteristic way from the signal shape measured with MMCs that have normal conducting absorbers [Lin07]. With those mainly two time constants are observed – one rise time and one decay time. In that case, the observed rise time on the order of 5 μs is limited by the readout electronics and the decay time $\tau = C_\mathrm{tot}/G$ is determined by the total heat capacity of the detector C_tot and the thermal conductance to the bath G[3]. For detectors with superconducting absorbers the pulse shape is much more complex and contains slow components, therefore the understanding of the pulse shape will be one key to any application involving superconducting absorbers.

Pulses for three different field generating persistent currents I were recorded at different temperatures of the experimental platform. By using the measured magnetization for a wide temperature range as discussed in section 5.3, for each of those measurements the temperature of the detector chip T_chip was calculated. In the next step, using the information of the theoretically expected slope of the flux change with temperature $\partial\Phi/\partial T$ at the chip temperature T_chip, the pulses recorded as flux signals $\Phi(t)$ were converted to temperature pulses $\Delta T(t)$. In order to parameterize the shape of these pulses, the function

$$\Delta T(t) = -\Delta T_0 e^{-t/\tau_0} + \Delta T_1 e^{-t/\tau_1} + \Delta T_2 e^{-t/\tau_2}, \tag{5.2}$$

was fitted to the data. This function is very similar to (5.1) but does not contain the first fast rise time τ_f. Instead the amplitude of the first rise can be deduced from the difference of the amplitude assigned to the rise and the amplitudes assigned to the decays as $\Delta T_\mathrm{f} = \Delta T_1 + \Delta T_2 - \Delta T_0$. Consequently, the fit was performed within a time interval Δt that does not start at the trigger time $t = 0$, but several fast time constants after the trigger time (typically about 120 μs), as depicted in Figure 5.7.

The results of this fitting procedure are summarized in Table 5.1. The obtained parameters are grouped according to the field generating currents. The table contains the measured temperature of the experimental platform as well as derived chip temperature T_chip. Furthermore, the temperature amplitudes ΔT_i as well as the corresponding time constants τ_i are shown. Additionally, the factor $\partial\Phi/\partial T$, used to convert the flux signal to a temperature pulse is given.
All time constants show an evident temperature dependence; with increasing temperature the underlying thermalization mechanisms become faster and thus the time constants decrease. Within the next section a thermal model for the thermalization is discussed and the data is analyzed with respect to this.

[3] An additional time pattern can only be observed for temperatures below 70 mK [Fle03].

I [mA]	T	T_{chip}	ΔT_0	τ_0	ΔT_1	τ_1	ΔT_2	τ_2	$\partial\Phi/\partial T$
94	34	58	41.3	0.413	45.2	1.573	2.3	14.778	1.040
ZFC	58	69	47.4	0.261	48.6	0.952	2.8	7.464	0.780
	78	83	53.7	0.158	51.3	0.637	2.6	5.917	0.540
69	34	58	41.3	0.445	44.3	1.669	2.4	14.031	0.800
FC	60	71	50.9	0.288	52.7	0.956	3.3	6.275	0.550
	78	83	53.7	0.183	53.9	0.615	3.2	4.673	0.410
54	33	56	43.1	0.469	45.8	1.587	2.5	10.102	0.650
ZFC	57	70	53.5	0.291	54.2	1.006	3.0	7.476	0.430
	78	83	55.7	0.164	53.7	0.616	2.3	4.884	0.300
54	33	56	41.5	0.493	43.4	1.722	2.3	12.986	0.650
FC	58	69	48.8	0.298	50.0	1.053	2.6	9.970	0.430
	78	83	50.0	0.172	49.7	0.651	2.7	5.144	0.300

Table 5.1 Results of the fitting procedure described in the text. The temperatures T are given in mK, all temperature amplitudes ΔT_i are given in μK and all time constants τ_i are given in ms. The conversion factor $\partial\Phi/\partial T$ is given in flux quanta per millikelvin $\Phi_0/\,\mathrm{mK}$. For some experiments the current was injected into the meander prior to cooling through T_c of rhenium (FC) and for some the current was injected below T_c of rhenium (ZFC).

5.4.3 Thermal Model

The physical reason for the observed time pattern of the signals recorded for X-rays absorbed in the superconducting rhenium as well as for superconducting absorbers in general is unknown so far. In the following an ansatz is presented to investigate the possible physical processes involved.
The model we assume consists of a reservoir and two thermal systems, the Au:Er sensor including the gold spacer[4] and the rhenium absorber as seen in Figure 5.8. The systems are characterized by their heat capacities C_r and C_s. The thermal link G_rs connects the absorber to the sensor. The sensor itself is linked to the thermal reservoir by the link G_sb. Solving the corresponding differential equations for this system with an instantaneous heat input into the absorber leads to a signal shape featuring two time constants, one rise time τ_0 and one decay time τ_1. The thermalization in the presence of a superconducting absorber is more complex, showing a time pattern with four time constants. Obviously this cannot be described by a thermal model as simple as just described. The model can of course be extended to reproduce a relaxation behavior with four time constants. However there is no unique way to achieve that. At present there is not even a most likely candidate that could be motivated by data discussed in the literature. In the following a possible model describing the thermalization is presented, a schematic of which is shown in Figure 5.8.
The thermal system, labeled as sensor consists of the Au:Er sensor as well as the gold

[4] In the following discussion when referring to the sensor this includes the Au:Er sensor as well as the gold spacer.

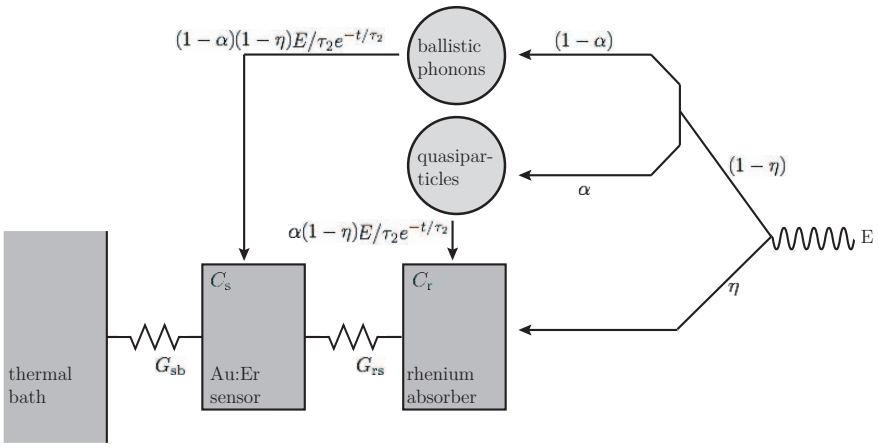

Figure 5.8 Schematic of a thermal model possibly describing the signal time pattern of a detector with a superconducting rhenium absorber.

spacer glued to it; the Kapitza resistance between those is assumed to be of minor importance. The second thermal system, labeled as absorber, comprises phonons and thermal excitations of quasiparticles across the superconducting gap, both of these contributions are assumed to be small at working temperature of the detector. Furthermore, the system might comprise normal metal regions or nuclei, where the latter are most likely interacting too slowly to be considered. Another possible contribution to the absorber system are so-called quasiparticles generated after the absorption of an X-ray. Quasiparticles are expected to have a rather long lifetime at the temperatures of interest. They might behave like a quasi-thermal system that can equilibrate with other thermal systems, like the phonons by absorbing and releasing energy.

Within the model we want to assume that the energy E, deposited in the superconducting rhenium absorber, is split up in three parts. The fraction ηE is directly absorbed by the thermal system of the absorber, while the remaining energy $(1-\eta)E$ is temporarily stored in two athermal systems. One is assigned to the quasiparticle system of the superconductor and absorbs $\alpha(1-\eta)$ of the total energy, later the quasiparticles release their energy content to the absorber with a time constant τ_2 and lead to the slow decay times of the signals. This process could be interpreted as quasiparticle recombination. As seen in the preceding section, the observed time constants are in the millisecond range. This would be much shorter than the theoretically expected recombination times in perfect single crystal superconductors at these temperatures, as mentioned in section 3.4.3. The remaining fraction $(1-\alpha)(1-\eta)$ of the energy is deposited into another athermal system that releases the energy on a short time scale to the sensor. The underlying process could be associated to ballistic phonons generated in an early phase of the downconversion of the initially produced energetic photoelectrons. A certain fraction of these phonons might freely propagate through the superconductor, cross the interface to the sensor and thermalize, herewith causing the fast rise of the observed signal.

The evolution of the sensor temperature in time can be described by two differential equations

$$\begin{aligned} \dot{T}_\mathrm{r} &= -\frac{G_\mathrm{rs}}{C_\mathrm{r}}(T_\mathrm{r}-T_\mathrm{s}) + \eta\frac{E}{C_\mathrm{r}}\delta(t) + \alpha(1-\eta)\frac{E}{C_\mathrm{r}}\frac{1}{\tau_2}e^{-t/\tau_2} \\ \dot{T}_\mathrm{s} &= -\frac{G_\mathrm{sb}}{C_\mathrm{s}}(T_\mathrm{s}-T_\mathrm{b}) - \frac{G_\mathrm{rs}}{C_\mathrm{s}}(T_\mathrm{s}-T_\mathrm{r}) + (1-\alpha)(1-\eta)\frac{E}{C_\mathrm{r}}\frac{1}{\tau_f}e^{-t/\tau_f}, \end{aligned} \tag{5.3}$$

here T_r, T_s and T_b are the temperatures of the rhenium absorber, the gold erbium sensor and the thermal bath, respectively. As the occurring temperature changes are small, the thermal conductances and heat capacities can be assumed to be constant. Within this approximation (5.3) can be solved with respect to T_s analytically, leading to a solution that can be written as follows

$$T_\mathrm{s}(t) - T_\mathrm{b} = -\Delta T_\mathrm{f} e^{-t/\tau_\mathrm{f}} - \Delta T_0 e^{-t/\tau_0} + \Delta T_1 e^{-t/\tau_1} + \Delta T_2 e^{-t/\tau_2}, \tag{5.4}$$

here the amplitudes ΔT_i as well as the time constants τ_i are cumbersome expressions of the deposited energy E, the thermal links G_rs and G_sb, the heat capacities C_r and C_s and the branching ratios of the energy η and α. The complete analytical solution can be found in appendix A.

Making use of these relations we can derive the parameters C_r, C_s , G_rs, G_sb, α, η and τ_2 of the thermal model from the fitting parameters given in Table 5.1, that describe the pulse shapes. Following this procedure we can indeed find unique solutions for the parameters τ_2, G_sb and $\alpha(1-\eta)$ for each pulse. However, the set of equations is not sufficient to uniquely determine all other parameters. One additional constraint is needed and in order to proceed from here, we want to assume that the thermodynamic properties of the Au:Er sensor as well as the gold spacer are well enough understood (see section 3.3.2) to fix the value of C_s to a calculated value $C_\mathrm{s}(T_\mathrm{chip}, I)$ for the given geometry. All necessary input parameters as well as the obtained results are summarized in Table 5.2.

In the following some observations are discussed. The fitted branching ratio η appears to be independent of injected field current and temperature. The averaged value extracted from the data for all different experimental conditions is $\eta = (66 \pm 3)\%$; this fraction of the energy is directly absorbed by the thermal system. The other branching ratio α, that describes how much of the energy is going into a system of ballistic phonons that directly thermalize in the sensor and what fraction is absorbed by the quasiparticles can also be evaluated in the same manner. This results to a value of $\alpha = (92 \pm 3)\%$. However, this result must be handled with more care as a systematic behavior can be observed. At this point of the discussion it needs to be mentioned that for higher temperatures the slower rise becomes very short and cannot be clearly distinguished from the initial fast rise. In the current method of data analysis this systematically leads to a suppression of the initial rise at higher temperatures and $\alpha \to 1$ is found in this limit. Combining both results for the branching ratios, the energy going into the quasiparticle system, given by $\alpha(1-\eta)E$, is almost constant with a value of (0.31 ± 0.02).

I [mA]	T_{chip}	C_{s}	C_{r}	G_{rs}	G_{sb}	α	η	τ_2
94	58	7.33	3.78	3.97	10.72	0.874	0.616	14.778
ZFC	69	6.71	3.20	5.02	17.23	0.919	0.65	7.464
	83	6.15	3.50	8.97	23.85	0.996	0.661	5.917
69	58	7.14	3.58	3.26	10.58	0.887	0.637	14.031
FC	71	6.50	2.46	3.47	16.73	0.894	0.668	6.275
	83	6.06	2.32	5.08	24.66	0.937	0.652	4.673
54	56	7.20	2.52	2.01	12.15	0.868	0.699	10.102
ZFC	70	6.48	2.78	4.00	15.38	0.923	0.671	7.476
	83	6.00	2.81	6.21	26.84	0.993	0.728	4.884
54	56	7.20	2.81	2.12	11.22	0.902	0.672	12.986
FC	69	6.48	2.91	4.08	14.74	0.931	0.623	9.970
	83	6.00	2.90	6.20	25.08	0.953	0.673	5.144

Table 5.2 Parameters derived from the fitting parameters in Table 5.1. The heat capacities C_{r} and C_{s} are given in units of pJK^{-1}, the thermal conductances G_{rs} and G_{sb} are given in $10^{-9}\mathrm{WK}^{-1}$.

As a further result the heat capacity C_{r} of the thermal degrees of freedom of the rhenium absorber is found to be on the order of $3\,\mathrm{pJK}^{-1}$. At a temperature of $T = 60\,\mathrm{mK}$ this would, e.g. correspond to a normal metal region in the rhenium with a volume of about $250\,\mu\mathrm{m} \times 250\,\mu\mathrm{m} \times 5\,\mu\mathrm{m}$, which is about 1% of the total absorber volume. A normal metal region of that size could possibly be explained by residual fields in the cryostat which where not sufficiently shielded at the position of the detector. The same normal conducting volume could also correspond to a 500nm thick surface layer distributed over all surfaces. A reason for such a behavior could be found in defects close to the crystal's surface. However, neither an evident temperature nor a magnetic field dependence of the absorber heat capacity C_{r} can be found in the data of Table 5.2. Here again, the increasing uncertainty of the fitting parameter α towards higher temperatures and the resulting trend $\alpha \to 1$ might cause a similar problem in determining C_{r}. In particular a systematic temperature dependence in this small temperature range might become faint.

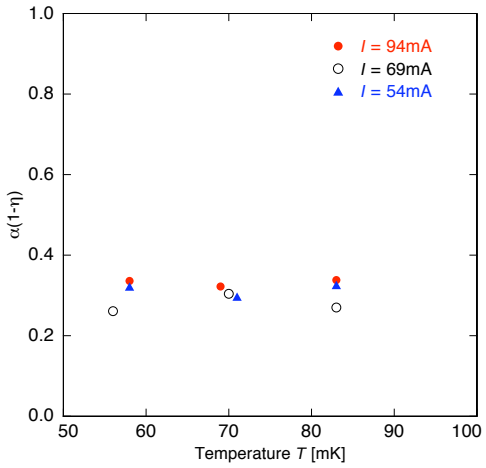

Figure 5.9 The figure shows the parameter $\alpha(1-\eta)$ extracted from the data as a function of chip-temperature.

In this analysis the thermal conductance between the rhenium absorber and the sensor comes out to be between $G_{\mathrm{rs}} = 2.0 \times 10^{-9}\,\mathrm{WK}^{-1}$ and $G_{\mathrm{rs}} = 9.0 \times 10^{-9}\,\mathrm{WK}^{-1}$. An increase with temperature is clearly observed, though no explicit power law can be seen. Interesting information can also be extracted from the values of the parameter G_{sb}, the thermal link between sensor and bath. As the energy E fed to the system can be described as

$$E = \int_0^\infty (T_{\mathrm{s}}(t) - T_{\mathrm{b}}) G_{\mathrm{sb}} dt, \tag{5.5}$$

G_{sb} is directly related to the time integral of the measured temperature pulse and the deposited energy E – being independent of details of the discussed model. Consequently this parameter also contains the information, if all incoming energy is detected or if some of it is stored in the quasiparticle system on a much longer time scale and is therefore not observable in the experimental pulse shapes.

The extracted thermal conductances range from $G_{\mathrm{sb}} = 1.1 \times 10^{-8}\,\mathrm{WK}^{-1}$ to $G_{\mathrm{sb}} = 2.7 \times 10^{-8}\,\mathrm{WK}^{-1}$ and they show a temperature dependence for all field currents that is proportional to T^x, where x varies from $x = 2.0$ to $x = 2.3$. As this thermal conductance should be limited by the Kapitza resistance between the sensor and the silicon substrate of the detector chip, a temperature dependence proportional to T^3 is expected. Recently [Lin07], the thermal conductance of a Au:Er–Si interface with a slightly different geometry was determined to be $G = 3.0 \times 10^{-6} T^3\,\mathrm{WK}^{-4}$, leading to a thermal conductance of $G = 0.65 \times 10^{-9}\,\mathrm{WK}^{-1}$ at a temperature of 60 mK. In this experiment a circular Au:Er sensor with a radius of $r = 25\,\mu\mathrm{m}$ was glued with the same epoxy on a silicon substrate. Considering the larger area of contact of $200\,\mu\mathrm{m} \times 200\,\mu\mathrm{m}$ in the present experiment, the thermal conductance would result to be $G_{\mathrm{sb}} = 1.3 \times 10^{-8}\,\mathrm{WK}^{-1}$. The averaged value extracted from the data at $T = 60\,\mathrm{mK}$ is $G_{\mathrm{sb}} = 1.1 \times 10^{-8}\,\mathrm{WK}^{-1}$. This shows a surprisingly good agreement of the interface resistance of glued contacts of two different detector setups. In principle it would be even more interesting for the understanding of the thermalization behavior of superconducting absorbers to reverse the presented analysis and to calculate the energy that leads to the temperature pulse by multiplying the area under the pulse and an independently determined value for G_{sb}. In this way it can be analyzed, how much of the deposited energy is indeed detected by the sensor. As mentioned before it would indeed be possible that a part of the deposited energy is stored in quasiparticles with long recombination times. However, this independent determination of G_{sb} was not possible with the detector developed within the framework of this thesis.

This almost naturally leads to an outlook towards further experiments that will provide more information about the thermalization within a superconductor. One possible experiment would consist of an MMC with a Au:Er sensor and a rhenium absorber that just partially covers the sensor. When a setup of that kind is exposed to X-rays two kinds of signals – firstly, resulting from the thermalization in a normal conductor and secondly, resulting from the thermalization in a superconductor – could be studied whereas all other experimental conditions are identical. The major

difference between the two types of signals would be the number of athermally generated quasiparticles, which should be negligible for X-rays absorbed in the normal metal sensor. A measurement of this kind will definitely enable us to answer the question whether or not a finite part of the deposited energy is stored in quasiparticle states with a long lifetime and therefore cannot be observed on the timescale of the detected signals. The true elegance of this experiment is that the analysis of the experimental data can be done without any of the assumptions needed above. As the operating temperature T_{chip}, the sensitivity $\mathrm{d}\Phi/\mathrm{d}T$ of the paramagnetic sensor and the thermal link G_{sb}between the sensor and the thermal bath are exactly the same for both types of events. The energies that give rise to both type of events can be compared by comparing the area underneath the pulses

$$E = \int_0^\infty (\Phi_{\mathrm{s}}(t)dt, \tag{5.6}$$

where the detector signal $\Phi_{\mathrm{s}}(t)$ is given in units of flux measured in the SQUID.

5.5 Optimization of a Future MMC for MARE

It has been mentioned before that the meander used within this work was not optimized with respect to signal to noise ratio. An optimization for a possible future detector was carried out for this purpose. As for any application some boundary conditions are assumed. In the present case a meander that is transformer coupled to a SQUID, as seen in Figure 3.13(a), is assumed. For a given SQUID, the meander geometry, as well as the sensor properties can be varied to optimize the energy resolution of the detector.

On the one hand, the expected signal size can be calculated from simulated magnetic field distributions given by the sensor geometry. The time constants of a detector signal need to be fixed explicitly. In order to define the spectral shape of the detector response upon the deposition of energy, we want to assume a signal rise time of 5 μs and a decay time of 5 ms. On the other hand, different noise contributions need to be considered. For a given SQUID the white noise level and the $1/f$ noise is assumed to be $\sqrt{S_\Phi} = 0.75\,\mu\Phi_0/\sqrt{\mathrm{Hz}}$ and $\sqrt{S_\Phi} = 3\,\mu\Phi_0/\sqrt{\mathrm{Hz}}$ at 1 Hz, respectively. Furthermore, the $1/f$ noise contribution usually observed in high resolution MMCs with Au:Er sensors is included in the optimization. The corresponding flux noise in the SQUID is characterized in Table 5.3 by its amplitude $\sqrt{S_{\Phi,1/f}}$ at a frequency of 1 Hz. Additionally, the thermodynamic energy fluctuations, as discussed in section 3.2, are taken into account with a spectral shape according to the assumed time constants.

Some boundary conditions are introduced before optimizing the signal to noise ratio. The assumed meander is made of niobium structures featuring a width $w = 4.25\,\mu$m and a pitch $p = 10\,\mu$m that are feasible to be produced in the in-house clean room. In order to assure that sensors with the well understood bulk properties can be produced, very thin sensors and sensors are excluded form the parameter

range. The lower limit of the sensor height h_s is set to 1.25 μm. For the MMC an absorber heat capacity of C_{abs}=1 pJK^{-1} at a temperature of T=50 mK is assumed, this is e.g. given by a gold absorber with the dimensions of 240 μm × 240 μm × 5 μm. For the data given in Table 5.3 this value is assumed to vary proportionally to the operating temperature. A chosen SQUID has an input inductance of L_i = 3.5 nH and a mutual inductance between the input coil and the SQUID of M_{is}=0.28 nH. A SQUID with these parameters has been chosen, because is has been successfully used at temperatures below 100 mK in numerous previous experiments.

The signal to noise ratio is numerically optimized as described in section 3.2, varying the generating field current I, the areas of the meander and the sensor A_s=A_m and the height of the sensor h_s. For each temperature T and concentration x the other parameters are optimized and an theoretically achievable energy resolution is calculated.

The results of this optimization can be seen in Table 5.3. In particular at a temperature of T = 40 mK an energy resolution of ΔE = 3.4 eV can for example be achieved with a sensor of an area of 254 μm × 254 μm, a height of 1.25 μm and an erbium concentration of 188 ppm. The optimized field generating current would be about 40 mA, this results in a sensor heat capacity of 1.26 pJK^{-1}. For this the $1/f$-noise contribution of the sensor would approximately be 2.8 $\mu\Phi_0/\sqrt{\text{Hz}}$ at a frequency of 1 Hz.

T [mK]	x [ppm]	ΔE [eV]	$\frac{d\Phi}{dE}$ $\left[\frac{\mu\Phi_0}{eV}\right]$	I [mA]	$\sqrt{A_s}$ [μm]	h_s [μm]	C_s $\left[\frac{pJ}{K}\right]$	$\sqrt{S_{\Phi,1/f}}$ $\left[\frac{\mu\Phi_0}{\sqrt{Hz}}\right]$
30	96	2.2	22.3	30	272.6	1.45	0.92	2.2
	188	2.2	23.3	30	216.4	1.25	1.07	2.5
	366	2.5	20.6	34.6	150..9	1.25	1.31	2.6
	683	2.9	16.1	46.5	100.0	1.25	1.48	2.2
	868	3.2	14.6	52.4	90.4	1.25	1.67	2.5
40	96	3.6	13.7	42.5	301.0	1.54	1.15	2.2
	188	3.4	15.6	40.1	254.7	1.25	1.26	2.8
	366	3.5	15.1	45.0	181.1	1.25	1.55	3.0
	683	4.0	12.7	56.6	125.1	1.25	1.92	3.0
	868	4.3	11.4	64.1	105.2	1.25	1.97	2.9
50	96	5.2	9.4	60.6	308.7	1.61	1.43	2.4
	188	4.7	11.3	53.3	274.9	1.27	1.49	3.0
	366	4.7	11.7	56.6	204.5	1.25	1.79	3.3
	683	5.2	10.2	68.9	139.1	1.25	2.11	3.3
	868	5.6	9.5	75.1	123.1	1.25	2.38	3.3

Table 5.3 Results of the optimization of energy resolution of a future MMC.

Besides the fact that the energy resolution of these detectors with transformer coupled readout is well suited for the requirements of a successful MARE experiment, this type of setup has a number of advantages:

- The microfabrication of the niobium structures can be done in the in-house cleanroom. This implies that the SQUIDs itself need no modifications whenever minor design changes of the detector chip are made.

- In particular the heater of the persistent current switch can be positioned further away from the detection loop. In that way the temperature of the rhenium absorber can be kept below T_c of rhenium while injecting currents into the meander.

- With the SQUID separated from the meander chip there is no power dissipation on the detector chip. Consequently, the temperature of the chip T_{chip} is closer to the bath temperature. As seen in the preceding sections this simplifies the analysis enormously and allows for a more stringent comparison of detector properties to the theoretical expectations. Furthermore, the chip temperature itself will be lower. As the results from the optimization show, this is generally suggested for a optimum detector performance.

6. Summary and Outlook

In the present work the development of a metallic magnetic calorimeter designed to measure the β-spectrum of ^{187}Re is presented and discussed. The shape of this spectrum can be used for the direct determination of the neutrino mass. To achieve this, the MARE project proposes the development of large detector arrays in order to obtain be sensitive to a neutrino mass of about $0.2\,\mathrm{eV/c^2}$, a value also proposed by the KATRIN experiment, which is currently under construction.

The low temperature detector developed within this work comprises of a paramagnetic temperature sensor located in a weak magnetic field, that is generated by a meander shaped coil. The material used as a sensor is gold doped with a concentration of 600 ppm of the rare earth metal erbium. A rhenium absorber, superconducting at the operation temperature of the detector, is well thermally coupled to the sensor. An energy deposition within the absorber leads to a temperature increase and therefore a change of magnetization of the sensor material that is detected as a change of flux in the sensing inductance of a low noise SQUID magnetometer.

So far, all micro-calorimeters for high resolution detection of β-particles and single X-rays discussed in literature that used superconductors with high Debye temperature, like rhenium, as absorbers, suffered from detector signals with long time constants which are generally believed to be related to long quasiparticle recombination times. A detailed understanding of the thermalization of superconductors and the acceleration of the recombination dynamics will be of major importance for the successful application of superconducting absorbers. Knowing the complexity of this topic it appears to be very helpful, if basic and important parameters that characterize the superconducting behavior of the absorber material, like its critical temperature T_c and the resistivity in the normal conducting state above T_c can be measured in situ.

Within the framework of this thesis it was shown that the critical temperature of rhenium single crystal absorbers of magnetic calorimeters can be studied in situ with two different methods. Firstly, the magnetic Johnson noise of the rhenium absorber is used to characterize the transition to superconductivity. As the amplitude and the spectral shape of the noise depends on the resistivity of the absorber material, not only the transition temperature T_c but also the resistivity in the normalconducting state can be determined with a reasonable precision. The latter only depending on the precise knowledge of the geometrical arrangement of the detector and the quality of the finite element simulations. Secondly, the superconducting transition can be seen by the change of another quantity, the voltage per flux quantum in the FLL mode of the SQUID electronics. A superconducting plane above the meander in the form of the rhenium absorber changes the mutual inductances between the meander shaped pick-up loop and the feedback coil of the SQUID, which is inversely proportional to the voltage per flux quantum. Both of these in situ measuring techniques indicate that the critical temperature of the prepared single crystals observed prior to a heat

treatment is about 1 K higher than the literature value of $T_c = 1.69\,\mathrm{K}$. The deviating transition temperature can be cured if the samples undergo a heat treatment for about one hour at a temperature of about 1900 K.

In a second set of experiments, the detector was exposed to a X-ray source. The detector signals upon the absorption of single X-rays are analyzed and show an evolution in time that can be described by four time constants, a signal shape that is much more complex than for MMCs with normal conducting absorbers. A possible thermal model consisting of two thermal and two athermal systems is proposed to describe the observed signal shape. The evolution of the sensor temperature in time can be characterized by six parameters, two heat capacities, two thermal conductances and two parameters describing the splitting of the incoming energy among the systems.

As a result the branching ratio of the energy appears to be a stable number. About two thirds of the energy is directly absorbed by the thermal system, the remaining energy is stored in the athermal systems associated to quasiparticles and ballistic phonons. Within this model the heat capacity of the rhenium absorber is found to be about 3 pJK^{-1}. It could be interpreted as a normal metal region adding up to about 1% of the absorber volume. However, a corresponding systematic dependence on temperature could not be observed. The thermal conductance between the Au:Er sensor and the silicon substrate connected to the thermal bath is also deduced in the analysis. The value is in good agreement compared to the determination of the thermal conductance between these materials achieved in a previous experiment. It turns out that this thermal conductance will be of further interest as it contains information whether all the energy introduced to the detector can actually be detected. A very promising experiment that makes use of this idea is suggested in the thesis.

As a first step towards faster recombination dynamics, detectors with a metallic interface between the superconducting absorber and the normal conducting sensor (or spacer) could be studied. An experiment of that kind is already in process. A further reduction of the quasiparticle recombination time might be achieved by the introduction of so-called quasiparticle traps, layers with smaller gap energy, between the absorber and the sensor. Furthermore, the recombination of quasiparticles might be sped up by reducing the energy gap itself. Doping superconductors with magnetic impurities is known to reduce the band gap. A first experiment, where the recombination times in manganese doped zinc are studied, is already planned[Gal07].

As soon as the problem of long relaxation times is solved and the signal shape is comparable to the one of present MMCs for high resolution X-ray detection featuring normalconducting absorbers, it seems very plausible, that since the heat capacities are of the same order of magnitude, also a similar energy resolution can be achieved. Recently developed X-ray detectors show an energy resolution of $\Delta E = 2.7\,\mathrm{eV}$. A detector with these properties would perfectly meet the requirements of the MARE project to achieve a detection limit for the neutrino mass on the level of $0.2\,\mathrm{eV/c^2}$.

A. Appendix

The thermal model assumed in section 5.4.3 leads to the following differential equations describing the evolution of the sensor temperature in time

$$\begin{aligned}
\dot{T}_\mathrm{r} &= -\frac{G_\mathrm{rs}}{C_\mathrm{r}}(T_\mathrm{r}-T_\mathrm{s}) + \eta\frac{E}{C_\mathrm{r}}\delta(t_0) + \alpha(1-\eta)\frac{E}{C_\mathrm{r}}\frac{1}{\tau_2}e^{-t/\tau_2} \\
\dot{T}_\mathrm{s} &= -\frac{G_\mathrm{sb}}{C_\mathrm{s}}(T_\mathrm{s}-T_\mathrm{b}) - \frac{G_\mathrm{rs}}{C_\mathrm{s}}(T_\mathrm{s}-T_\mathrm{r}) + (1-\alpha)(1-\eta)\frac{E}{C_\mathrm{r}}\frac{1}{\tau_f}e^{-t/\tau_f},
\end{aligned} \tag{A.1}$$

here T_r, T_s and T_b are the temperatures of the rhenium absorber, the gold erbium sensor and the thermal bath, respectively. In the case where the occurring temperature changes are small the thermal conductances and heat capacities are assumed to be constant. The differential equations can be solved with respect to T_s analytically, leading to a solution that can be written as follows

$$T_\mathrm{s}(t) - T_\mathrm{b} = -\Delta T_\mathrm{f} e^{-t/\tau_\mathrm{f}} - \Delta T_0 e^{-t/\tau_0} + \Delta T_1 e^{-t/\tau_1} + \Delta T_2 e^{-t/\tau_2}. \tag{A.2}$$

The amplitudes ΔT_i are expressions of the deposited energy E, the thermal conductances G_rs and G_sb, the heat capacities C_r and C_s and the branching ratios of the energy η and α and can be written as:

$$\begin{aligned}
\Delta T_\mathrm{f} &= \frac{-\tau_1\tau_0}{(\tau_1-\tau_f)(\tau_0-\tau_f)}(1-\eta)(1-\alpha)(\tau_f G_\mathrm{rs} - C_\mathrm{r})\frac{E}{C_\mathrm{r}C_\mathrm{s}} \\
\Delta T_0 &= \frac{\tau_1\tau_0}{\tau_1-\tau_0}\left[\frac{(1-\eta)(1-\alpha)(\tau_0 G_\mathrm{rs} - C_\mathrm{r})}{\tau_0-\tau_\mathrm{f}} + \eta G_\mathrm{rs} + \frac{\alpha G_\mathrm{rs}\tau_0(1-\eta)}{\tau_0-\tau_2}\right]\frac{E}{C_\mathrm{r}C_\mathrm{s}} \\
\Delta T_1 &= \frac{\tau_1\tau_0}{\tau_1-\tau_0}\left[\frac{(1-\eta)(1-\alpha)(\tau_1 G_\mathrm{rs} - C_\mathrm{r})}{\tau_1-\tau_\mathrm{f}} + \eta G_\mathrm{rs} + \frac{\alpha G_\mathrm{rs}\tau_1(1-\eta)}{\tau_1-\tau_2}\right]\frac{E}{C_\mathrm{r}C_\mathrm{s}} \\
\Delta T_2 &= \frac{\tau_1\tau_0}{(\tau_1-\tau_2)(\tau_0-\tau_2)}\alpha(1-\eta)\tau_2 G_\mathrm{rs}\frac{E}{C_\mathrm{r}C_\mathrm{s}}
\end{aligned}$$

Furthermore, the time constants τ_0 and τ_1 can be expressed using the two heat capacities C_r and C_s and the two thermal conductances G_rs and G_sb as follows:

$$\begin{aligned}
\frac{1}{\tau_0} &= \frac{1}{2C_\mathrm{r}C_\mathrm{s}}\left[C_\mathrm{r}(G_\mathrm{sb}+G_\mathrm{rs}) + C_\mathrm{s}G_\mathrm{rs} + \sqrt{(C_\mathrm{r}(G_\mathrm{sb}+G_\mathrm{rs}) - C_\mathrm{s}G_\mathrm{rs})^2 + 4C_\mathrm{r}C_\mathrm{s}G_\mathrm{rs}^2}\right] \\
\frac{1}{\tau_1} &= \frac{1}{2C_\mathrm{r}C_\mathrm{s}}\left[C_\mathrm{r}(G_\mathrm{sb}+G_\mathrm{rs}) + C_\mathrm{s}G_\mathrm{rs} - \sqrt{(C_\mathrm{r}(G_\mathrm{sb}+G_\mathrm{rs}) - C_\mathrm{s}G_\mathrm{rs})^2 + 4C_\mathrm{r}C_\mathrm{s}G_\mathrm{rs}^2}\right].
\end{aligned}$$

Bibliography

[Abr70] A. Abragam and B. Bleaney. Electron paramagnetic resonance of transition metals. *Claredon Press Oxford*, 1970.

[And07] E. Andreotti et al. MARE, Microcalorimeter Arrays for a Rhenium Experiment: A detector overview; Frontier Detectors for Frontier Physics - Proceedings of the 10th Pisa Meeting on Advanced Detectors. *Nucl. Instr. Meth. A*, 572(1):208–210, 2007.

[Ban93] S. R. Bandler, C. Enss, R. E. Lanou, H. J. Maris, T. More, F. S. Porter and G. M. Seidel. Metallic magnetic bolometers for particle detection. *J. Low Temp. Phys.*, V93(3):709–714, 1993.

[Bon02] J. Bonn, B. Bornschein, L. Bornschein, B. Flatt, Ch. Kraus, E. W. Otten, J. P. Schall, Th. Thummler and Ch. Weinheimer. Limits on neutrino masses from tritium β-decay;. *Nuclear Physics B - Proceedings Supplements*, 110:395–397, 2002.

[Bur04] A. Burck. Entwicklung großflächiger magnetischer Kalorimeter zur energieaufgelösten Detektion von Röntgenquanten und hochenergetischen Teilchen. Master's thesis, Kirchhoff-Institut für Physik, Universität Heidelberg, 2004.

[Chu68] C. W. Chu, T. F. Smith and W. E. Gardner. Superconductivity of rhenium and some rhenium-osmium alloys at high pressure. *Phys. Rev. Lett.*, 20(5):198–201, Jan 1968.

[Cla04] J. Clarke and A.I. Braginski, editors. *The SQUID Handbook: Fundamentals and Technology of SQUIDs and SQUID Systems*, volume 1. Wiley-VCH Verlag Weinheim, 2004.

[Con93] E. Cosulich, F. Gatti and S. Vitale. Further results on μ-calorimeters with superconducting absorber. *J. Low Temp. Phys.*, V93(3):263–268, 1993.

[Cow56] C.L. Cowan Jr., F. Reines, F.B. Harrison, H.W. Kruse and A.D. MacGuire. Detection of the free neutrino: a confirmation. *Science*, 124:103–104, July 1956.

[Dan05] T. Daniyarov. *Metallische magnetische Kalorimeter zum hochauflösenden Nachweis von Röntgenquanten und hochenergetischen Molekülen.* PhD thesis, Kirchhoff-Institut für Physik, Universität Heidelberg, 2005.

[Dav73] D. Davidov, C. Rettori, A. Dixon, K. Baberschke, E. P. Chock and R. Orbach. Crystalline-field effects in the electron-spin resonance of rare earths in the noble metals. *Phys. Rev. B*, 8(8):3563–3568, Oct 1973.

[Ens05] C. Enss and S. Hunklinger. *Low-Temperature Physics*. Springer-Verlag Berlin Heidelberg, 2005.

[Fle00] A. Fleischmann, C. Enss, J. Schönefeld, J. Sollner, K. Horst, J. S. Adams, Y. H. Kim, G. M. Seidel, and S. R. Bandler. The sensitivity of magnetic calorimeters with large heat capacity;. *Nucl. Instr. Meth. A*, 444(1-2):100–103, 2000.

[Fle03] A. Fleischmann. *Magnetische Mikrokalorimeter: Hochauflösende Röntgenspektroskopie mit energiedispersiven Detektoren*. PhD thesis, Kirchhoff-Institut für Physik, Universität Heidelberg, 2003.

[Fle05] A. Fleischmann, C. Enss and G. M. Seidel. *Metallic Magnetic Calorimeters*, volume 99 of *Topics Appl. Phys.*, pages 151–216. Springer-Verlag Berlin Heidelberg, 2005.

[Gal07] G. Gallinaro, Universitá di Genova. Private communication.

[Gat99] F. Gatti, F. Fontanelli, M. Galeazzi, A. M. Swift and S. Vitale. Detection of environmental fine structure in the low-energy β-decay spectrum of ^{187}Re. *Nature*, 397(6715):137–139, 1999.

[GHa71] P. E. Gregers-Hansen, M. Krusius, and G. R. Pickett. Sign of the nuclear quadrupole interaction in rhenium metal. *Phys. Rev. Lett.*, 27(1):38–41, Jul 1971.

[Hah92] W. Hahn, M. Loewenhaupt and B. Frick. Crystal field excitations in dilute rare earth noble metal alloys. *Physica B*, Volumes 180-181:176–178, June 1992.

[Har68] J. T. Harding and J. E. Zimmerman. Quantum interference magnetometry and thermal noise from a conducting environment;. *Physics Letters A*, 27(10):670–671, 1968.

[Hau06] D. Haug. Entwicklung eines magnetischen Kalorimeters zur Neutrinomassenbestimmung aus dem Endpunkt des β-Spektrums von ^{167}Re. Master's thesis, Kirchhoff-Institut für Physik, Universität Heidelberg, 2006., 2006.

[Hor99] Karsten Horst. Hochauflösende Rötgenspektroskopie mit kalorimetrischen Tieftemperaturdetektoren basieren auf ^{166}Erbium-dotiertem Gold. Master's thesis, Kirchhoff-Institut für Physik, Universität Heidelberg, 1999.

[Hul57] J. K. Hulm and B. B. Goodman. Superconducting properties of rhenium, ruthenium, and osmium. *Phys. Rev.*, 106(4):659–671, May 1957.

[Irw05] K. D. Irwin and G. C. Hilton. *Transition-Edge Sensors*, volume 99 of *Topics Appl. Phys.*, pages 63–150. Springer-Verlag Berlin Heidelberg, 2005.

[Kap76] S. B. Kaplan, C. C. Chi, D. N. Langenberg, J. J. Chang, S. Jafarey and D. J. Scalapino. Quasiparticle and phonon lifetimes in superconductors. *Phys. Rev. B*, 14(11):4854–4873, Dec 1976.

[Kit06] C. Kittel. *Einführung in die Festkörperphysik*. R. Oldenbourg Verlag, München, 2006.

[Koo91] Steven E. Koonin. Environmental fine structure in low-energy β-particle spectra. *Nature*, 354(6353):468–470, 1991.

[Koz00] A. G. Kozorezov, A. F. Volkov, J. K. Wigmore, A. Peacock, A. Poelaert, and R. den Hartog. Quasiparticle-phonon downconversion in nonequilibrium superconductors. *Phys. Rev. B*, 61(17):11807–11819, May 2000.

[Koz00b] A. G. Kozorezov. Kinetics of interacting quasiparticles and phonons in non-equilibrium superconductors;. *Nucl. Instr. Meth. A*, 444(1-2):3–7, 2000.

[Lin07] Markus Linck. *Entwicklung eines metallischen magnetischen Kalorimeters für die hochauflösende Röntgenspektroskopie*. PhD thesis, Kirchhoff-Institut für Physik, Universität Heidelberg, 2007.

[Lob85] V. M. Lobashev and P. E. Spivak. A method for measuring the electron antineutrino rest mass;. *Nucl. Instr. Meth. A*, 240(2):305–310, 1985.

[Lob03] V. M. Lobashev. The search for the neutrino mass by direct method in the tritium β-decay and perspectives of study it in the project katrin;. *Nuclear Physics A*, 719:C153–C160, 2003.

[Mak62] Z. Maki, M. Nakagawa, and S. Sakata. Remarks on the unified model of elementary particles. *Prog. Theor. Phys.*, 28:870, 1962.

[Mar06] F. Gatti et al. MARE - Microcalorimeter Arrays for a Rhenium Experiment. Proposal, unpublished. Online verision: http://crio.mib.infn.it/wig/silicini/proposal/proposal_MARE_v2.6.pdf.

[McC85] D. McCammon. A New Technique for Neutrino Mass Measurement. In V. Barger and D. Cline, editors, *Neutrino Mass and Low Energy Weak Interactions*, pages 329–, 1985.

[McC05] D. McCammon. *Semiconductor Thermistors*, volume 99 of *Topics Appl. Phys.*, pages 35–62. Springer-Verlag Berlin Heidelberg, 2005.

[Nuc04] A. Nucciotti, C. Arnaboldi, C. Brofferio, et al. How to improve the sensitivity of future neutrino mass experiments with thermal calorimeters; proceedings of the 10th international workshop on low temperature detectors. *Nucl. Instr. Meth. A*, 520(1-3):148–150, 2004.

[Pau30] Offener Brief an die Gruppe der Radioaktiven bei der Gauvereinstagung zu Tübingen. Collected Scienetific Papers by W. Pauli, (published by R. Kronig and V.F. Weisskopf, 1964, p. 159).

[Phi64] Norman E. Phillips. Low-temperature heat capacities of gallium, cadmium, and copper. *Phys. Rev.*, 134(2A):A385–A391, Apr 1964.

[Rid65] O.D. McMasters, P.E. Rider, K.A. Gschneidner Jr. Gold-rich rare-earth-gold solid solutions. *Transactions of the Metallurgical Society of Aime*, 233:1488, 1965.

[Raz03] M. Razeti. *Study on microcalorimetric detectors for neutrino mass measurement with sensitivity in the eV/c^2 range*. PhD thesis, Universitá di Genova, 2003.

[Rou04] Esteban Roulet. Neutrino phenomenology. 2004.

[San06] S. Sangiorgio. The microcalorimeter arrays for a Rhenium experiment (MARE): A next-generation calorimetric neutrino mass experiment based on the study of ^{187}Re β-spectrum; International Workshop of Nuclear Physics 27th course - Neutrinos in Cosmology, in Astro, Particle and Nuclear Physics. *Progress in Particle and Nuclear Physics*, 57(1):68–70, 2006.

[Sch00] J. Schönefeld. *Entwicklung eines mikrostrukturierten magnetischen Tieftemperaturkalorimeters zum hochauflösenden Nachweis von einzelnen Röntgenquanten*. PhD thesis, Kirchhoff-Institut für Physik, Universität Heidelberg, 2000.

[Sha67] J. K. N. Sharma. Heat conductivities below 1K, I. *Cryogenics*, 7(1-4):141–156, 1967.

[Sis04] M. Sisti, C. Arnaboldi, C. Brofferio, et al. New limits from the milano neutrino mass experiment with thermal microcalorimeters; proceedings of the 10th international workshop on low temperature detectors. *Nucl. Instr. Meth. A*, 520(1-3):125–131, 2004.

[Sjo75] M. E. Sjöstrand and G. Seidel. Hyperfine resonance properties of Er^{3+} in Au. *Phys. Rev. B*, 11(9):3292–3297, May 1975.

[Smi70] David R. Smith and P. H. Keesom. Specific heat of rhenium between 0.15 and 4.0 K. *Phys. Rev. B*, 1(1):188–192, Jan 1970.

[Tes77] Claudia D. Tesche and John Clarke. dc-SQUID: Noise and optimization. *J. Low Temp. Phys.*, V29(3):301–331, 1977.

[Uml88] E. Umlauf and M. Bühler. A magnetic bolometer for single particle detection. *Europhys. Lett.*, 5(4):297–301, 1988.

[Vit84] G. Torelli, P. Delpiaz, G. Fiorentini, editor. *Proceedings of the International School of Physics of Exotic Atoms*, number 23, 423, 1985., Enrice, 1984. published in Fundamental Interaction in Low-Energy Systems.

[Wil69] Gwyn Williams and L. L. Hirst. Crystal-field effects in solid solutions of rare earths in noble metals. *Phys. Rev.*, 185(2):407–415, Sep 1969.

[Win07] Mark Winter. WebElements^{TM}, the periodic table on the WWW; www.webelements.com, 2007.

Acknowledgments

There are many people who I would like to thank for the role they played, be it academic or otherwise, in making this project both possible and enjoyable. My extended personal gratitude goes to:

- Professor Christian Enss for kindly welcoming me in his exciting group.
- Special thanks go to Loredana Gastaldo and Andreas Fleischmann for their support and day-to-day supervision. Additional gratitude is due for the enormous amounts of time dedicated to the completion of this work.
- All the Bolos accompanying me and the rhenium project over the last year: Andreas Burck, Daniel Haug, Christian Höhn, Sebastian Kempf, Stefan Lausberg, Markus Linck, Hannes Rotzinger, Sönke Schäfer – thank you!
- All the No-Bolos: Masoomeh Baszrafshan, Gudrun Fickenscher, Gernot Kasper, Florian Klotz, Lena Maerten (or are you a Bolo?), Astrid Netsch, Mihai Petrovici, Stefanie Riegel and Manfred von Schickfus – though mostly not sharing the same lab, I appreciated your sympathy for dying SQUIDs and I really enjoyed the extended coffee hours.
- Andreas Reiser for his support in polishing tiny crystals and bearing any question concerning liquefiers.
- Thomas Wolf and Dieter Weiskat for the technical and friendly provision of sputtered rhenium cuboids and a beautiful current source, respectively.
- My friends and fellow students for having a good time here and everywhere we meet.

Finally, I want to thank my long suffering parents for their unlimited support and all the provided advice and my brother Sven for his well known last minute help.